Exploring the partonic phase at finite chemical potential within an extended off-shell transport approach

Pierre Moreau,[1,*] Olga Soloveva,[1] Lucia Oliva,[1,2] Taesoo Song,[2] Wolfgang Cassing,[3] and Elena Bratkovskaya[1,2]

[1]*Institute for Theoretical Physics, Johann Wolfgang Goethe Universität, Frankfurt am Main, 60438, Germany*
[2]*GSI Helmholtzzentrum für Schwerionenforschung GmbH, Darmstadt, 64291, Germany*
[3]*Institut für Theoretische Physik, Universität Gießen, 35392, Germany*

We extend the parton-hadron string dynamics (PHSD) transport approach in the partonic sector by explicitly calculating the total and differential partonic scattering cross sections as a function of temperature T and baryon chemical potential μ_B on the basis of the effective propagators and couplings from the dynamical quasiparticle model (DQPM) that is matched to reproduce the equation of state of the partonic system above the deconfinement temperature T_c from lattice QCD. We calculate the collisional widths for the partonic degrees of freedom at finite T and μ_B in the timelike sector and conclude that the quasiparticle limit holds sufficiently well. Furthermore, the ratio of shear viscosity η over entropy density s, i.e., η/s, is evaluated using the collisional widths and compared to lattice QCD calculations for $\mu_B = 0$ as well. We find that the novel ratio η/s does not differ very much from that calculated within the original DQPM on the basis of the Kubo formalism. Furthermore, there is only a very modest change of η/s with the baryon chemical μ_B as a function of the scaled temperature $T/T_c(\mu_B)$. This also holds for a variety of hadronic observables from central $A + A$ collisions in the energy range $5\,\text{GeV} \leqslant \sqrt{s_{NN}} \leqslant 200\,\text{GeV}$ when implementing the differential cross sections into the PHSD approach. We only observe small differences in the antibaryon sector ($\bar{p}$, $\bar{\Lambda} + \bar{\Sigma}^0$) at $\sqrt{s_{NN}} = 17.3\,\text{GeV}$ and $200\,\text{GeV}$ with practically no sensitivity of rapidity and p_T distributions to the μ_B dependence of the partonic cross sections. Small variations in the strangeness sector are obtained in all collisional systems studied ($A + A$ and C + Au); however, it will be very hard to extract a robust signal experimentally. Since we find only small traces of a μ_B dependence in heavy-ion observables—although the effective partonic masses and widths as well as their partonic cross sections clearly depend on μ_B—this implies that one needs a sizable partonic density and large space-time QGP volume to explore the dynamics in the partonic phase. These conditions are only fulfilled at high bombarding energies where μ_B is, however, rather low. On the other hand, when decreasing the bombarding energy and thus increasing μ_B, the hadronic phase becomes dominant and accordingly it will be difficult to extract signals from the partonic dynamics based on "bulk" observables.

I. INTRODUCTION

Nonequilibrium many-body theory or transport theory has become a major topic of research in nuclear physics, cosmological particle physics, and condensed matter physics. The multidisciplinary aspect arises due to a common interest in understanding the various relaxation phenomena of quantum dissipative systems. Important questions in nuclear and particle physics at the highest energy densities are the following: (i) how do nonequilibrium systems in extreme environments evolve and eventually thermalize, (ii) what are the macroscopic transport coefficients of the matter in equilibrium, and (iii) what is the nature of possible phase transitions? The dynamics of heavy-ion collisions at various bombarding energies provide the laboratory of choice for research on nonequilibrium quantum many-body physics and relativistic quantum-field theories, since the initial state of a collision resembles an extreme nonequilibrium configuration while the final state might even exhibit some degree of thermalization.

For many decades, the powerful method of the Schwinger-Keldysh [1–4] or closed time path (CTP) real-time Green's functions—being the essential degrees of freedom—has been shown to provide an appropriate basis for the formulation of the complex problems in the various areas of nonequilibrium quantum many-body physics. Within this framework, one can derive suitable approximations depending on the problem under consideration by preserving overall consistency relations [5]. Originally, the resulting causal Dyson-Schwinger equation of motion for the one-particle Green's functions (or two-point functions), i.e., the Kadanoff-Baym (KB) equations [6], have served as the underlying scheme for deriving various transport phenomena and generalized transport equations. For review articles on the Kadanoff-Baym equations in the various areas of nonequilibrium quantum physics, we refer the reader to Refs. [7–12].

On the other hand, kinetic transport theory is a convenient method to study many-body nonequilibrium systems. Kinetic equations, which do play the central role in more or less all

*moreau@fias.uni-frankfurt.de

practical simulations, can be derived from the KB equations within suitable approximations. Hence, a major impetus in the past has been to derive semiclassical Boltzmann-like transport equations within the standard quasiparticle approximation. Additionally, off-shell extensions by means of a gradient expansion in the space-time inhomogeneities—as already introduced by Kadanoff and Baym [6]—have been formulated for various directions in physics, from a relativistic electron-photon plasma [13] to the transport of nucleons at intermediate heavy-ion reactions [14] to the transport of partons in high-energy heavy-ion reactions [15–23]. We recall that on the formal level of the KB equations the various forms assumed for the self-energy have to fulfill consistency relations in order to preserve symmetries of the fundamental Lagrangian [6,24,25]. This allows for a unified treatment of stable and unstable (resonance) particles also out of equilibrium.

The possibilities of solving in particular QCD in Minkowski space for out-of-equilibrium configurations and nonvanishing quark (or baryon) densities will be low in the next years, such that effective approaches are necessary to model the dominant properties of QCD in equilibrium, i.e., the thermodynamic quantities and transport coefficients. To this aim, the dynamical quasiparticle model (DQPM) has been introduced [26], which is based on partonic propagators with sizable imaginary parts of the self-energies incorporated. Whereas the real part of the self-energies can be attributed to a dynamically generated mass (squared), the imaginary parts contain the information about the interaction rates in the system [27–34]. Furthermore, the imaginary parts of the propagators define the spectral functions of the degrees of freedom which might show narrow (or broad) quasiparticle peaks [35]. A further advantage of a propagator-based approach is that one can formulate a consistent thermodynamics [36] as well as a causal theory for nonequilibrium configurations on the basis of KB equations.

In order to explore the phase diagram of strongly interacting matter as a function of temperature T and baryon chemical potential μ_B, different strategies are employed at present: (i) Lattice calculations of quantum chromodynamics (lQCD) [37–39] show that the phase transition from hadronic to partonic degrees of freedom (at vanishing baryon chemical potential $\mu_B = 0$) is a crossover. This phase transition is expected to turn into a first-order transition at a critical point (T_r, μ_r) in the phase diagram with increasing baryon chemical potential μ_B [40–42]. Furthermore, a nonvanishing magnetic field, as produced in heavy-ion collisions, can also influence the position of the critical point [43]. Since this latter cannot be determined theoretically in a reliable way by lQCD calculations, experimental information from relativistic nucleus-nucleus collisions has to be obtained. In this respect, (ii) the beam energy scan (BES) program—performed at the relativistic heavy-ion collider (RHIC)—aims to find the critical point and the phase boundary by gradually decreasing the collision energy [44,45] and thus increasing the average baryon chemical potential. Additionally, new facilities such as the Facility for Antiproton and Ion Research (FAIR) and Nuclotron-based Ion Collider fAcility (NICA) are under construction to explore in particular the intermediate energy

range of $4 \text{ GeV} \leqslant \sqrt{s_{NN}} \leqslant 20 \text{ GeV}$, where one might study also the competition between chiral symmetry restoration and deconfinement [46,47].

Accordingly, the partonic and hadronic dynamics at finite or large baryon densities (or chemical potentials) are of actual interest and are addressed also in various hydrodynamical models [48–51], hydrodynamical + hadron transport models [52–54], and more parametric approaches [55]. However, as found in Ref. [52], the inclusion of baryon diffusion leads only to a small effect on the "bulk" observables at BES RHIC energies.

About a decade ago, the parton-hadron string dynamics (PHSD) transport approach was introduced, which differs from the conventional Boltzmann-type models in the aspect [56] that the degrees of freedom for the QGP phase are off-shell massive strongly interacting quasiparticles that generate their own mean-field potential. The masses of the dynamical quarks and gluons in the QGP are distributed according to spectral functions whose pole positions and widths, respectively, are defined by the real and imaginary parts of their self-energies [57]. The partonic propagators and self-energies, furthermore, are defined in the DQPM in which the strong coupling and the self-energies are fitted to lattice QCD results [26], assuming an ansatz for the mass and width dependencies on temperature T and quark chemical potential μ_q inspired by the hard-thermal-loop (HTL) approach.

In the past, the PHSD transport model, based on temperature-dependent DQPM masses, widths, and cross sections [58], has successfully described numerous experimental data in relativistic heavy-ion collisions from the Alternating Gradient Synchrotron (AGS), Super-Proton Synchrotron (SPS), RHIC, and Large Hadron Collider (LHC) energies [56,57,59–64].

The goals of this study are to explore on a microscopic level the partonic phase at finite baryonic chemical potential μ_B and different temperatures T and to find traces of the μ_B dependence in observables. Although the extension of the DQPM model to finite baryon chemical potentials has been realized previously [65,66] and the (T, μ_B) dependence of the transport coefficients (such as shear and bulk viscosities or electric conductivity) for the equilibrated QGP matter have been calculated [65,66], the properties of the nonequilibrium QGP at finite μ_B—as created in heavy-ion collisions (HICs)—were not addressed by microscopic calculations within the PHSD so far in a consistent fashion.

Although the DQPM inherits the information on the total interaction rates of the degrees of freedom in terms of widths, it lacks the individual total as well as differential cross sections for different reaction channels with partons that are needed in the collision terms of a consistent relativistic transport approach. In PHSD, these cross sections have been parametrized so far to comply with the individual widths of quarks, antiquarks, and gluons as a function of energy density (cf. Ref. [58]), which can be related to the temperature T by the lQCD equation of state (EoS). In this study, we will calculate these total and differential cross sections in leading order for the individual partonic channels on the basis of the DQPM propagators and couplings. This will allow us to

additionally explore the energy and angular dependence of partonic cross sections on their T and μ_B dependence.

Moreover, using these cross sections, we calculate the interaction rates of quarks and gluons in the timelike sector to study the validity of the quasiparticle approximation. Furthermore, we evaluate the equilibrium shear viscosity $\eta(T, \mu_B)$ within the Kubo formalism and the relaxation time approximation (RTA) and compare to results from lQCD at $\mu_B = 0$ for the ratio η/s. The calculated total and differential cross sections as well as parton masses—depending on (T, μ_B)—have been implemented in the PHSD and thus we introduce a further step toward a consistent relativistic transport approach in the partonic sector.

In order to extract the Lagrange parameters μ_B and T from the PHSD in heavy-ion collisions, we developed a practical method (based on the expansion of thermodynamic quantities in terms of the baryon number susceptibilities) which allows us to relate the energy density and baryon densities—calculated in each cell in space-time during heavy-ion collisions—to a state-of-the-art lattice QCD EoS (practically identical to the DQPM EoS at small μ_B).

Finally, we will search for traces of the μ_B dependence in the QGP dynamics in "bulk" observables from relativistic heavy-ion collisions such as rapidity distributions and p_T spectra using the extended PHSD approach as a working tool.

This paper is organized as follows: In Sec. II, we will provide a brief reminder of the DQPM and its ingredients as well as its results for the partonic equation of state. Section III will be devoted to the calculation of the partonic differential cross sections as a function of T and μ_B, employing the effective propagators and couplings from the DQPM. In Sec. IV, we will use these cross sections to evaluate partonic scattering rates for fixed T and μ_B as well as compute transport coefficients in Sec. V like the shear viscosity η in comparison to calculations from lQCD at $\mu_B = 0$. Section VI is devoted to the extraction of the local T and μ_B in the actual transport approach and characteristic results will be presented for central collisions of $Pb + Pb$ at $\sqrt{s_{NN}} = 17.3$ and $Au + Au$ 200 GeV. In Sec. VII, we will compare the results of the novel transport approach PHSD5.0 to those of PHSD4.0 and experimental data for central heavy-ion collisions from AGS to RHIC energies. Furthermore, we explore the sensitivity of rapidity distributions and transverse momentum spectra to the partonic scattering in asymmetric $C + Au$ collisions at the top SPS and RHIC energies. A summary of our study will be presented in Sec. VIII, while technical details in the calculation of the matrix elements and differential cross sections are shifted to the Appendixes.

II. REMINDER OF THE DQPM AND ITS INGREDIENTS

Early concepts of the quark-gluon plasma (QGP) were guided by the idea of a weakly interacting system of massless partons which might be described by perturbative QCD (pQCD). However, experimental observations at RHIC indicated that the new medium created in ultrarelativistic $Au + Au$ collisions is interacting more strongly than hadronic matter. It is presently widely accepted that this medium is a strongly interacting system of partons as extracted experimentally from

the strong radial expansion and the scaling of the elliptic flow $v_2(p_T)$ of mesons and baryons with the number of constituent quarks and antiquarks [67]. At vanishing chemical potential μ_B, the QCD problem can be addressed at zero and finite temperature by lattice QCD calculations on a $(3 + 1)$-dimensional torus with a suitable discretization of the QCD action on the Euclidean lattice. These calculations so far have provided valuable information on the QCD equation of state, chiral symmetry restoration, and various correlators that can be attributed or related to transport coefficients. Because of the Fermion sign problem, lQCD calculations at finite μ_B are presently not robust and one has to rely on nonperturbative—but effective—models to obtain information in the (T, μ_B) plane or for systems out of equilibrium.

A. Quasiparticle properties

As mentioned above, in the KB theory the field quanta are described in terms of dressed propagators with complex self-energies [26]. Whereas the real part of the self-energies can be related to mean-field potentials (of Lorentz scalar, vector, or tensor type), the imaginary parts provide information about the lifetime and/or reaction rates of timelike particles. The determination and extraction of complex self-energies for the partonic degrees of freedom can be performed within the DQPM by fitting lattice QCD calculations in thermal equilibrium.

The basic ideas of the DQPM are as follows:

   (i) Introduce an ansatz (with a few parameters) for the (T and μ_B) dependence of masses and widths of the dynamical quasiparticles (quarks, antiquarks, and gluons) to define the self-energies.
  (ii) Define the form of propagators for strongly interacting massive partons.
 (iii) Evaluate the QGP thermodynamics in equilibrium using the Kadanoff-Baym (KB) theory and calculate (in the 2PI approximation) the entropy density s and other thermodynamic quantities such as the pressure P and energy density.
 (iv) Compare the DQPM results with the lQCD ones at zero and finite μ_B and T and fix the initial parameters to obtain the best reproduction of the lQCD thermodynamics.

This defines the properties of the quasiparticles, their propagators and couplings.

We recall the main ingredients of the DQPM:

(1) The DQPM postulates retarded propagators of the quark and gluon degrees-of-freedom (for the QGP in equilibrium) in the form

$$G^R(\omega, \mathbf{p}) = \frac{1}{\omega^2 - \mathbf{p}^2 - M^2 + 2i\gamma\omega} \tag{1}$$

using $\omega = p_0$ for energy.

(2) The coupling (squared) g^2, which is the essential quantity in the DQPM defining the strength of the interaction and enters the definition of the DQPM thermal masses and widths, is extracted from lQCD. In our previous studies [68–70], we used an ansatz for the (T, μ_B) dependence of the

coupling $g^2 = \alpha_s/(4\pi)$ and extracted the two parameters—entering the parametrization of g^2—from a global fit to the lQCD thermodynamics. Furthermore, g^2 was also compared to quenched QCD results on $\alpha_s(T)$ at $\mu_B = 0$ for the pure glue case ($N_f = 0$) from Ref. [71].

Here we follow alternatively a procedure similar to Refs. [65,66] to determine the effective coupling (squared) g^2 as a function of temperature T; i.e., the coupling is defined at $\mu_B = 0$ by a parametrization of the entropy density from lattice QCD in the following way:

$$g^2(s/s_{SB}) = d((s/s_{SB})^e - 1)^f \quad (2)$$

with the Stefan-Boltzmann entropy density $s_{SB}^{QCD} = 19/9\pi^2 T^3$ and the parameters $d = 169.934$, $e = -0.178434$, and $f = 1.14631$. In the following, we use a parametrization of the entropy density at $\mu_B = 0$ calculated by lQCD from Refs. [72,73] to determine the DQPM coupling constant as a function of temperature.

The extension to finite μ_B can be worked out in different scenarios. First of all, an expansion of the grand-canonical potential, i.e., the negative pressure P, in terms of μ_B/T can be performed and the expansion coefficients can be calculated by lQCD [74,75]. This provides a solid framework for small and moderate μ_B. Alternatively, Maxwell relations can be employed to extract the thermodynamic potential at finite μ_B starting from the information given by lQCD at $\mu_B = 0$ [76]. Both methods give almost the same results up to $\mu_B \approx 450$ MeV [76]. For practical purposes, the explicit results can be fitted by a scaling ansatz [66] which works up to $\mu_B \approx 450$ MeV and suggests that the phase transition to the QGP is a crossover up to such baryon chemical potentials. We mention that the experimental studies of the STAR Collaboration within the BES program down to bombarding energies of $\sqrt{s_{NN}} = 7.7$ GeV—corresponding to $\mu_B \approx 450$ MeV—did not indicate any critical point in the QCD phase diagram [77] so far.

To obtain the coupling constant at finite baryon chemical potential μ_B, the scaling hypothesis assumes that g^2 is a function of the ratio of the effective temperature $T^* = \sqrt{T^2 + \mu_q^2/\pi^2}$ and the μ_B-dependent critical temperature $T_c(\mu_B)$ as [78]

$$g^2(T/T_c, \mu_B) = g^2\left(\frac{T^*}{T_c(\mu_B)}, \mu_B = 0\right) \quad (3)$$

with $\mu_B = 3\mu_q$ and $T_c(\mu_B) = T_c\sqrt{1 - \alpha\mu_B^2}$, where T_c is the critical temperature at vanishing chemical potential (≈ 0.158 GeV) and $\alpha = 0.974$ GeV^{-2}.

In Fig. 1, the DQPM running coupling $\alpha_s = g^2(T, \mu_B)/(4\pi)$ is displayed as a function of the scaled temperature $T/T_c(\mu_B)$ for different values of the baryon chemical potential μ_B. We find that with increasing μ_B the effective coupling drops in the vicinity of the critical temperature $T_c(\mu_B)$. This drop is rather moderate up to $\mu_B = 0.4$ GeV (adequate for central Au + Au collisions at 30 A GeV) but becomes significant for $\mu_B = 0.6$ GeV (roughly adequate for central Au + Au collisions at 10 A GeV). A comparison to the lattice results for quenched QCD
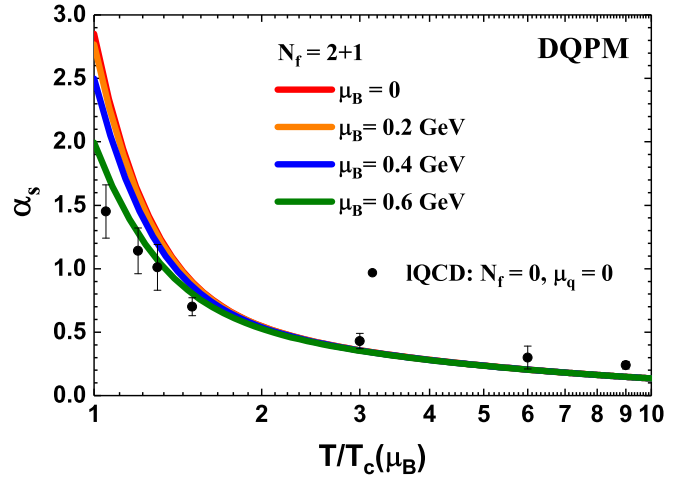
FIG. 1. The DQPM running coupling $\alpha_s = g^2(T, \mu_B)/(4\pi)$ (for $N_f = 2 + 1$) as a function of the scaled temperature $T/T_c(\mu_B)$ for different values of the baryon chemical potential μ_B. The lattice results for quenched QCD (for $N_f = 0$) are taken from Ref. [71] and scaled by the critical temperature $T_c \approx 270$ MeV.

from Ref. [71]—scaled by $T_c \approx 270$ MeV—shows that the DQPM coupling qualitatively matches the lattice results but is slightly larger for lower μ_B. We note, however, that this comparison should be taken only for orientation since the DQPM coupling corresponds to unquenched QCD with three light flavors ($N_f = 2 + 1$) whereas the lattice results are for quenched QCD ($N_f = 0$). Note that—since the running coupling (squared) $g^2 \sim (11N_c - 2N_f)^{-1}$ ($N_c = 3$)—the coupling is larger for a finite number of flavors N_f compared to $N_f = 0$.

With the coupling g^2 fixed from lQCD, one can now specify the dynamical quasiparticle mass (for gluons and quarks) which is assumed to be given by the HTL thermal mass in the asymptotic high-momentum regime, i.e., for gluons by [57,79]

$$M_g^2(T, \mu_B) = \frac{g^2(T, \mu_B)}{6}\left[\left(N_c + \frac{1}{2}N_f\right)T^2 + \frac{N_c}{2}\sum_q \frac{\mu_q^2}{\pi^2}\right] \quad (4)$$

and for quarks (antiquarks) by

$$M_{q(\bar{q})}^2(T, \mu_B) = \frac{N_c^2 - 1}{8N_c}g^2(T, \mu_B)\left(T^2 + \frac{\mu_q^2}{\pi^2}\right), \quad (5)$$

where $N_c = 3$ stands for the number of colors while $N_f (= 3)$ denotes the number of flavors. The dynamical masses (5) in the QGP are large compared to the bare masses of the light (u, d) quarks and adopted in the form (5) for the (u, d) quarks. The strange quark has a larger bare mass, which also enters to some extent the dynamical mass $M_s(T)$. This essentially suppresses the channel $g \to s + \bar{s}$ relative to the channel $g \to u + \bar{u}$ or $d + \bar{d}$ and controls the strangeness ratio in the QGP. Empirically, we have used $M_s(T, \mu_B) = M_u(T, \mu_B) + \Delta M = M_d(T, \mu_B) + \Delta M$, where $\Delta M = 30$ MeV, which has been fixed once in comparison to experimental data for the K^+/π^+ ratio in central Au + Au collisions at $\sqrt{s_{NN}} = 200$ GeV.

Furthermore, the effective quarks, antiquarks, and gluons in the DQPM have finite widths, which are adopted in the form [57]

$$
\gamma_g(T, \mu_B) = \frac{1}{3} N_c \frac{g^2(T, \mu_B) T}{8\pi} \ln\left[\frac{2c}{g^2(T, \mu_B)} + 1\right], \quad (6)
$$

$$
\gamma_{q(\bar{q})}(T, \mu_B) = \frac{1}{3} \frac{N_c^2 - 1}{2N_c} \frac{g^2(T, \mu_B) T}{8\pi} \ln\left[\frac{2c}{g^2(T, \mu_B)} + 1\right], \quad (7)
$$

where $c = 14.4$ is related to a magnetic cutoff, which is an additional parameter of the DQPM. Furthermore, we assume that the width of the strange quark is the same as that for the light (u, d) quarks.

The physical processes contributing to the width γ_g are both $gg \leftrightarrow gg$, $gq \leftrightarrow gq$ scattering as well as splitting and fusion reactions $gg \leftrightarrow g$, $gg \leftrightarrow ggg$, $ggg \leftrightarrow gggg$, or $g \leftrightarrow q\bar{q}$, etc. On the fermion side, elastic fermion-fermion scattering $pp \leftrightarrow pp$, where p stands for a quark q or antiquark $\bar{q}$, fermion-gluon scattering $pg \leftrightarrow pg$, gluon bremsstrahlung $pp \leftrightarrow pp + g$, or quark-antiquark fusion $q\bar{q} \leftrightarrow g$, etc., emerge. Note, however, that the explicit form of (6) is derived for hard two-body scatterings only. Furthermore, the widths $\gamma_{q(\bar{q})}(T)$ and $\gamma_g(T)$ provide only information on the total interaction rates and not on the individual differential cross sections. The computation of these cross sections will be carried out here in leading order on the basis of the propagators (1) and coupling (2) and (3) in Sec. III, which in turn will allow us to recalculate the widths (6) and (7) and explore the validity of the quasiparticle limit in the timelike sector.

B. Spectral functions

In line with the propagator (1), the parton spectral functions (or imaginary parts of the propagator $\rho = -2\,\mathrm{Im}\,G^R$) are no longer δ functions in the invariant mass squared but given by

$$
\rho_j(\omega, \mathbf{p}) = \frac{\gamma_j}{\tilde{E}_j}\left[\frac{1}{(\omega - \tilde{E}_j)^2 + \gamma_j^2} - \frac{1}{(\omega + \tilde{E}_j)^2 + \gamma_j^2}\right]
$$
$$
\equiv \frac{4\omega\gamma_j}{\left(\omega^2 - \mathbf{p}^2 - M_j^2\right)^2 + 4\gamma_j^2\omega^2} \quad (8)
$$

separately for quarks, antiquarks, and gluons $(j = q, \bar{q}, g)$. Here, $\tilde{E}_j^2(\mathbf{p}) = \mathbf{p}^2 + M_j^2 - \gamma_j^2$, where the widths γ_j and masses M_j from the DQPM have been described above. The spectral function (8) is antisymmetric in ω and normalized as [80]

$$
\int_{-\infty}^{\infty} \frac{d\omega}{2\pi} \omega \rho_j(\omega, \mathbf{p}) = \int_0^{\infty} \frac{d\omega}{2\pi} 2\omega\rho_j(\omega, \mathbf{p}) = 1, \quad (9)
$$

as mandatory for quantum field theory.
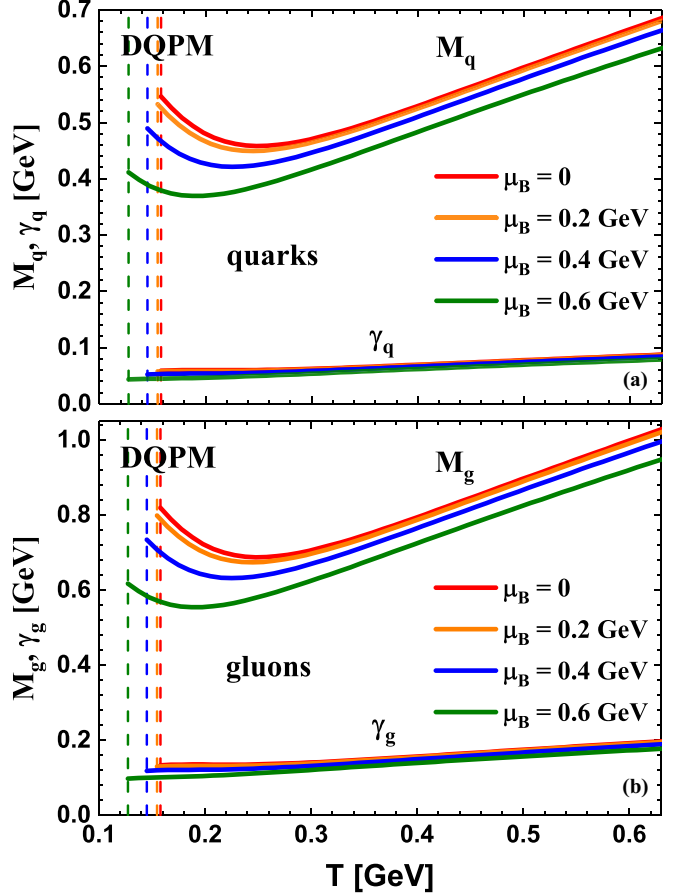
FIG. 2. The effective quark (a) and gluon (b) masses M and widths γ [from the parametrizations (6) and (7)] as a function of the temperature T for different μ_B. The vertical dashed lines correspond to the DQPM μ_B-dependent critical temperature $T_c(\mu_B)$.

The actual quark mass M_q and width γ_q—employed as input in the PHSD calculations—as well as the gluon mass M_g and width γ_g are depicted in Fig. 2 as a function of T/T_c and show an infrared enhancement close to T_c. For $\mu_q = \mu_B/3 = 0$, the DQPM gives

$$
M_q = \tfrac{2}{3}M_g, \quad \gamma_q = \tfrac{4}{9}\gamma_g. \quad (10)
$$

C. Thermodynamics within the DQPM

With the quasiparticle properties (or propagators) chosen as described above, one can evaluate the entropy density $s(T, \mu_B)$, the pressure $P(T, \mu_B)$, and energy density $\epsilon(T, \mu_B)$ in a straightforward manner by starting with the entropy density and number density in the propagator representation from Baym [36,81],

$$
s^{dqp} = -\int \frac{d\omega}{2\pi} \frac{d^3p}{(2\pi)^3} \left\{ d_g \frac{\partial n_B}{\partial T}[\mathrm{Im}\,(\ln -\Delta^{-1}) + \mathrm{Im}\,\Pi\,\mathrm{Re}\,\Delta] + \sum_{q=u,d,s} d_q \frac{\partial n_F(\omega - \mu_q)}{\partial T}\left[\mathrm{Im}\left(\ln -S_q^{-1}\right) + \mathrm{Im}\,\Sigma_q\,\mathrm{Re}\,S_q\right] \right.
$$
$$
\left. + \sum_{\bar{q}=\bar{u},\bar{d},\bar{s}} d_{\bar{q}} \frac{\partial n_F(\omega + \mu_q)}{\partial T}\left[\mathrm{Im}\left(\ln -S_{\bar{q}}^{-1}\right) + \mathrm{Im}\,\Sigma_{\bar{q}}\,\mathrm{Re}\,S_{\bar{q}}\right] \right\}, \quad (11)
$$

$$n^{dqp} = -\int \frac{d\omega}{2\pi} \frac{d^3p}{(2\pi)^3} \left\{ \sum_{q=u,d,s} d_q \frac{\partial n_F(\omega - \mu_q)}{\partial \mu_q} \left[\mathrm{Im}\left(\ln -S_q^{-1}\right) + \mathrm{Im}\,\Sigma_q\,\mathrm{Re}\,S_q \right] \right.$$

$$\left. + \sum_{\bar{q}=\bar{u},\bar{d},\bar{s}} d_{\bar{q}} \frac{\partial n_F(\omega + \mu_q)}{\partial \mu_q} \left[\mathrm{Im}\left(\ln -S_{\bar{q}}^{-1}\right) + \mathrm{Im}\,\Sigma_{\bar{q}}\,\mathrm{Re}\,S_{\bar{q}} \right] \right\} \tag{12}$$

where $n_B(\omega) = [\exp(\omega/T) - 1]^{-1}$ and $n_F(\omega - \mu_q) = \{\exp[(\omega - \mu_q)/T] + 1\}^{-1}$ denote the Bose-Einstein and Fermi-Dirac distribution functions, respectively, while $\Delta = (p^2 - \Pi)^{-1}$, $S_q = (p^2 - \Sigma_q)^{-1}$, and $S_{\bar{q}} = (p^2 - \Sigma_{\bar{q}})^{-1}$ stand for the full (scalar) quasiparticle propagators of gluons g, quarks q, and antiquarks $\bar{q}$. In Eqs. (11) and (12), Π and $\Sigma = \Sigma_q \approx \Sigma_{\bar{q}}$ denote the (retarded) quasiparticle self-energies. Furthermore, the number of transverse gluonic degrees of freedom is $d_g = 2 \times (N_c^2 - 1)$ while for the fermion degrees of freedom we use $d_q = 2 \times N_c$ and $d_{\bar{q}} = 2 \times N_c$.

In principle, Π as well as Δ are Lorentz tensors and should be evaluated in a nonperturbative framework. The DQPM treats these degrees of freedom as independent scalar fields (for each color and spin projection) with scalar self-energies which are assumed to be identical for quarks and antiquarks. This is expected to hold well for the entropy and number density. Note that one has to treat quarks and antiquarks separately in Eqs. (11) and (12) as their abundance differs at finite quark chemical potential $\mu_q = \mu_B/3$.

With the choice (8), the complex self-energies $\Pi = M_g^2 - 2i\omega\gamma_g$ and $\Sigma_q = M_q^2 - 2i\omega\gamma_q$ are fully defined via (4), (5), (6), and (7). Note that the retarded propagator (1) resembles the propagator of a damped harmonic oscillator (with an additional $\mathbf{p}^2$) and preserves microcausality also for $\gamma > M$ [82], i.e., in case of overdamped motion. Although the ansatz for the parton propagators is not QCD, it has been shown that a variety of QCD observables on the lattice are compatible with this choice [57].

In case the real and imaginary parts of the propagators Δ and S are fixed, the entropy density (11) and number density (12) can be evaluated numerically. As we deal with a grand-canonical ensemble, the Maxwell relations give

$$s = \frac{\partial P}{\partial T}, \quad n_B = \frac{\partial P}{\partial \mu_B}, \tag{13}$$

such that the pressure can be obtained by integration of the entropy density s over T and of the baryon density n_B over μ_B as

$$P(T, \mu_B) = P(T_0, 0) + \int_{T_0}^{T} s(T', 0)\, dT'$$

$$+ \int_0^{\mu_B} n_B(T, \mu_B')\, d\mu_B', \tag{14}$$

where one identifies the full entropy density s and baryon density n_B with the quasiparticle entropy density s^{dqp} (11) and baryon density $n_B = n^{dqp}/3$ (12). The starting point T_0 for the integration in T is chosen between $0.1 < T < 0.15$ GeV

where the entropy density is taken in accordance to the lattice QCD results from Ref. [73] in the hadronic sector.

The energy density ϵ then follows from the thermodynamical relation

$$\epsilon = Ts - P + \mu_B n_B \tag{15}$$

and thus is also fixed by the entropy $s(T, \mu_B)$ and baryon density $n_B(T, \mu_B)$ as well as the interaction measure

$$I := \epsilon - 3P = Ts - 4P + \mu_B n_B \tag{16}$$

that vanishes for massless and noninteracting degrees of freedom at $\mu_B = 0$.

A direct comparison of the resulting entropy density $s(T)$ (11), pressure $P(T)$ (14), energy density $\epsilon(T)$ (15), and interaction measure (16) from the DQPM with lQCD results from the BMW group [72,73] at $\mu_B = 0$ (a) and $\mu_B = 400\,\mathrm{MeV}$ (b) is presented in Fig. 3. The dimensionless results s/T^3, P/T^4, and ϵ/T^4 are shown to demonstrate the scaling with temperature. The agreement is sufficiently good for the entropy and energy density as well as for the pressure. A satisfactory agreement also holds for the dimensionless interaction measure, i.e., $(\epsilon - 3P)/T^4$ (cf. orange line in Fig. 3).

III. DIFFERENTIAL CROSS SECTIONS FOR PARTONIC INTERACTIONS

A. Definitions

1. On-shell case

The differential cross section for a $2 \to 2$ process of on-shell particles ($1 + 2 \to 3 + 4$) is given by

$$d\sigma^{\mathrm{on}} = \frac{d^3 p_3}{(2\pi)^3 2E_3} \frac{d^3 p_4}{(2\pi)^3 2E_4}$$

$$\times (2\pi)^4 \delta^{(4)}(p_1 + p_2 - p_3 - p_4) \frac{|\bar{\mathcal{M}}|^2}{F}, \tag{17}$$

where the flux is defined by $F = v_{\mathrm{rel}}\, 2E_1\, 2E_2$ with the definition $v_{\mathrm{rel}} = |\vec{v}_1 - \vec{v}_2|$ and the on-shell energies for the particle are defined as $E_j = \sqrt{\mathbf{p}_j^2 + M_j^2}$. $|\bar{\mathcal{M}}|^2$ denotes the matrix element squared averaged over the color and spin of the incoming particles and summed over those of the final particles. We want to evaluate the cross section in the rest frame of the heat bath where the Fermi-Dirac or Bose-Einstein functions describe the particle distributions. The only factor in Eq. (17) which is not Lorentz invariant is the flux factor F, while the other factors, the Lorentz-invariant phase space (LIPS), the matrix element $|\bar{\mathcal{M}}|^2$, and the δ function for energy-momentum conservation, are invariant. This implies that the cross section can be calculated in any frame, but the
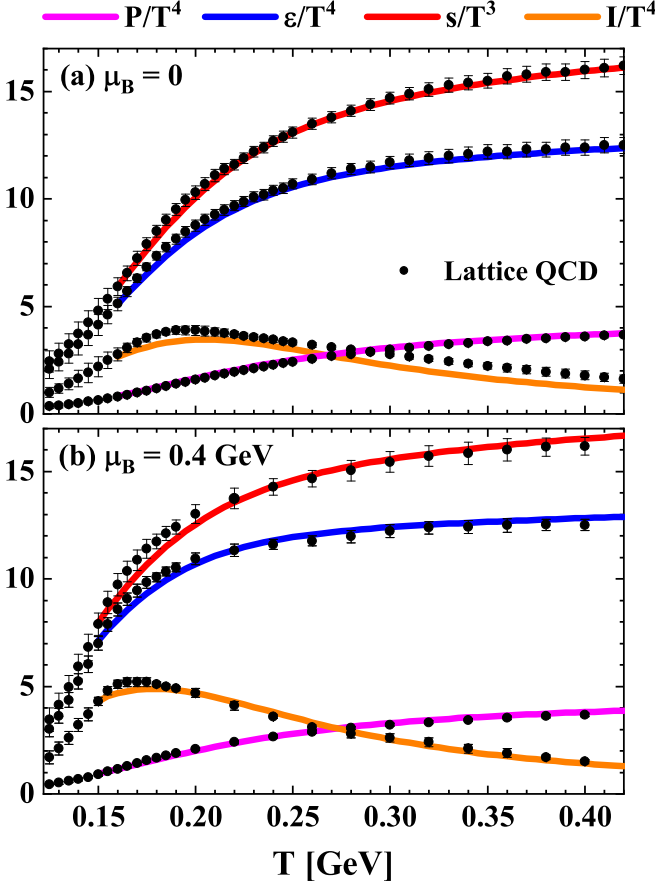
FIG. 3. The scaled pressure $P(T)/T^4$ (pink line), entropy density $s(T)/T^3$ (red line), scaled energy density $\epsilon(T)/T^4$ (blue line), and interaction measure (16) (orange line), from the DQPM in comparison to the lQCD results from Refs. [72,73] (full dots) for $\mu_B = 0$ (a) and $\mu_B = 400$ MeV (b).

flux factor has to be correctly taken into account according to the actual frame of interest.

The cross section is usually evaluated in the center-of-mass (c.m.) frame of the collision for simplicity. In this case, the momenta of the colliding particles obey $\mathbf{p_1} + \mathbf{p_2} = \mathbf{p_3} + \mathbf{p_4} = \mathbf{p} = \vec{0}$, and the notation $|\mathbf{p_1}| = |\mathbf{p_2}| = p_i$ and $|\mathbf{p_3}| = |\mathbf{p_4}| = p_f$ is used. The flux factor becomes $F^{\text{c.m.}} = 4p_i\sqrt{s}$ and, after simplification, Eq. (17) reads

$$d\sigma_{\text{on}}^{\text{c.m.}} = \frac{p_f\, d\Omega}{16\pi^2\sqrt{s}} \frac{|\bar{\mathcal{M}}|^2}{F^{\text{c.m.}}} = \frac{d\Omega}{64\pi^2 s} \frac{p_f}{p_i} |\bar{\mathcal{M}}|^2, \qquad (18)$$

where s in the Mandelstam variable and $d\Omega$ is the differential solid angle corresponding to one of the final particle. The momenta of the initial (i) and final particles (f) in the c.m. frame is found to be

$$p_{i,f} = \frac{\sqrt{[s - (M_{i,f} + M'_{i,f})^2][s - (M_{i,f} - M'_{i,f})^2]}}{2\sqrt{s}}, \qquad (19)$$

with $M_{i,f}$ and $M'_{i,f}$ being the masses of the colliding partons. The total cross section is obtained by performing the integral

in Eq. (18) over $d\Omega$ as

$$\sigma_{\text{on}}^{\text{c.m.}} = \frac{1}{32\pi s} \frac{p_f}{p_i} \int_{-1}^{1} d\cos(\theta)|\bar{\mathcal{M}}|^2, \qquad (20)$$

where θ is the final polar angle of one of the final particle in the c.m. frame. In the c.m. frame, the collision is independent from the azimuthal angle ϕ and the corresponding integration gives a factor 2π.

2. Off-shell case

In the off-shell case, the energy of the partons, as well their momenta, are independent degrees of freedom and a general definition of an "off-shell cross section" is not possible due to the lack of asymptotically stable states. However, transition matrix elements for different incoming and outgoing 4-momenta can be well defined also off shell. By transforming the Lorentz-invariant phase space in Eq. (17), one can include the off-shell effects for the scattering of timelike particles—in the case of a well-defined incoming flux $F = v_{\text{rel}}\, 2\omega_1\, 2\omega_2$—by integrating over the energy of the final timelike particles as

$$F d\sigma^{\text{off}} = \frac{d^4 p_3}{(2\pi)^4} \frac{d^4 p_4}{(2\pi)^4} \tilde{\rho}_3(\omega_3, \mathbf{p_3})\, \theta(\omega_3)\, \tilde{\rho}_4(\omega_4, \mathbf{p_4})\, \theta(\omega_4)$$
$$\times (2\pi)^4 \delta^{(4)}(p_1 + p_2 - p_3 - p_4)|\bar{\mathcal{M}}|^2 \qquad (21)$$

with the renormalized timelike spectral functions

$$\tilde{\rho}_j(\omega_j, \mathbf{p_j}) = \frac{\rho(\omega_j, \mathbf{p_j})\, \theta(p_j^2)}{\int_0^\infty \frac{d\omega_j}{(2\pi)} 2\omega_j\, \rho(\omega_j, \mathbf{p_j})\, \theta(p_j^2)}, \qquad (22)$$

where the spectral function ρ_i in (22)—corresponding to the parton type i—is taken from Eq. (8). The final parton masses are defined as $m_i^2 = p_i^2 = \omega_i^2 - \mathbf{p}_i^2$, where p_i is the 4-momentum of particle i. One can verify that by replacing the spectral functions by their on-shell value:

$$\lim_{\gamma_j \to 0} \rho_j(\omega, \mathbf{p}) = 2\pi\, \delta(\omega^2 - \mathbf{p}^2 - M_j^2)$$
$$= \frac{\pi}{\omega}\left[\delta\left(\omega - \sqrt{\mathbf{p}^2 + M_j^2}\right) + \delta\left(\omega + \sqrt{\mathbf{p}^2 + M_j^2}\right)\right], \qquad (23)$$

the off-shell cross section leads to the on-shell one as defined in the previous subsection from Eq. (17).

We follow the same strategy as in the previous subsection and evaluate the differential "off-shell cross section" for timelike quanta in the center-of-mass system of the collision for convenience. By making use of the δ function in Eq. (21), one can integrate over $d^4 p_4$ to obtain the total cross section in the c.m. frame by performing the integrations with the appropriate boundaries as

$$F^{\text{c.m.}} \sigma_{\text{off}}^{\text{c.m.}} = \frac{1}{(2\pi)^3} \int_0^{\sqrt{s}/2} p_f^2\, dp_f\, d\cos(\theta)$$
$$\times \int_{p_f}^{\sqrt{s}-p_f} d\omega_3^{\text{c.m.}} \tilde{\rho}_3(\omega_3, \mathbf{p_3})\, \tilde{\rho}_4(\omega_4, \mathbf{p_4})\, |\bar{\mathcal{M}}|^2 \qquad (24)$$

for $F^{\text{c.m.}} = 4p_i^{\text{c.m.}}\sqrt{s}$. Bear in mind that even if the calculation of the cross section is performed in the center-of-mass system,
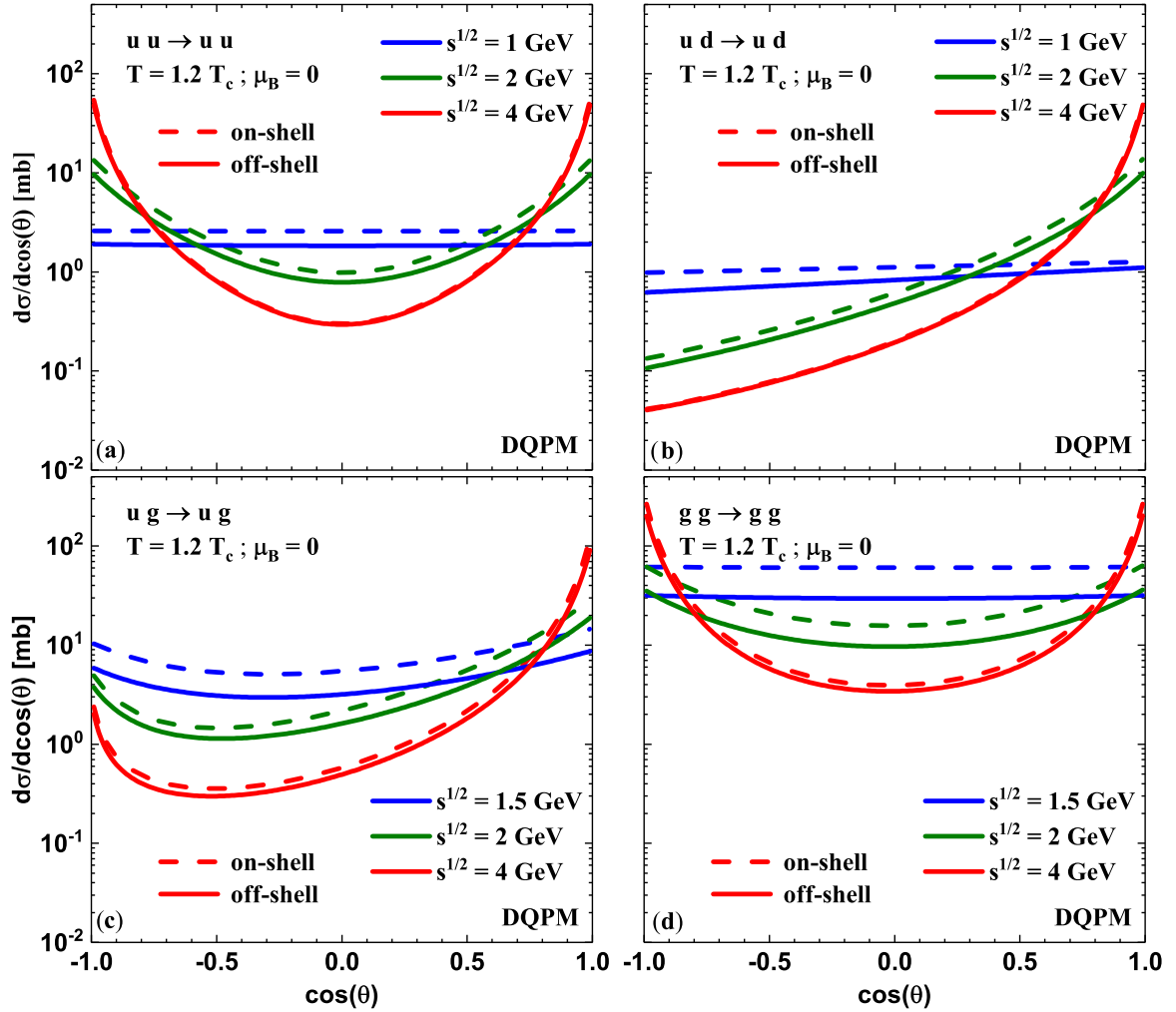
FIG. 4. Elastic differential cross sections between different partons for the on-shell case (dashed lines) from Eq. (18) and the off-shell case (solid lines) evaluated in the center of mass of the collision system as a function of the angle $\cos(\theta)$ between the initial and final momenta of one of the partons for $T = 1.2 T_c$ and $\mu_B = 0$. The initial masses of the colliding partons are taken as the pole masses from Eqs. (4) and (5). The different lines correspond to different collision energies $\sqrt{s}$ from 1 to 4 GeV (see legend).

the energies and momenta entering the spectral functions (8) should be expressed in the heat bath frame by applying the appropriate Lorentz transformations.

We mention that one can simplify the off-shell energy integration by an integration over the final masses of the partons in the nonrelativistic limit. The off-shell cross section from Eq. (21) then becomes [68]

$$\sigma_{\text{off}}^{\text{BW}} = \int_0^{\sqrt{s}} dm_3 \int_0^{\sqrt{s}-m_3} dm_4 \, \rho^{\text{BW}}(m_3) \, \rho^{\text{BW}}(m_4) \int d\sigma_{\text{on}}^{\text{c.m.}},$$
(25)

where the Breit-Wigner spectral function ρ^{BW} in Ref. [68] is obtained from Eq. (8) in the limit $\omega \to m$:

$$\rho_i^{\text{BW}}(m) = \frac{2}{\pi} \frac{2m^2 \gamma_i}{(m^2 - M_i^2)^2 + (2m\gamma_i)^2}.$$
(26)

This distribution fulfills the normalization $\int_0^\infty dm \, \rho^{\text{BW}}(m) = 1$.

B. Partonic scattering

In the framework of the DQPM, quarks and gluons are massive with a finite lifetime associated to their interaction width. In order to calculate the matrix elements corresponding to a scattering of DQPM partons, the scalar propagator (1) has to be replaced by the following propagators—with full Lorentz structure—to describe a massive vector gluon and massive (spin-1/2) fermion with a finite width [68]:

$$\mu, a \,\, \text{oooooooooo} \,\, \nu, b = -i\delta_{ab} \frac{g^{\mu\nu} - q^\mu q^\nu / M_g^2}{q^2 - M_g^2 + 2i\gamma_g q_0},$$
(27)

$$i \xrightarrow{\quad q \quad} j = i\delta_{ij} \frac{\slashed{q} + M_q}{q^2 - M_q^2 + 2i\gamma_q q_0},$$
(28)

where q is the 4-momentum of the exchanged particle. The δ functions ensure that the exchanged quark or gluon is conncted with other parts of the diagram with the same color (a, b for the gluon and i, j for the quark). The invariant matrix
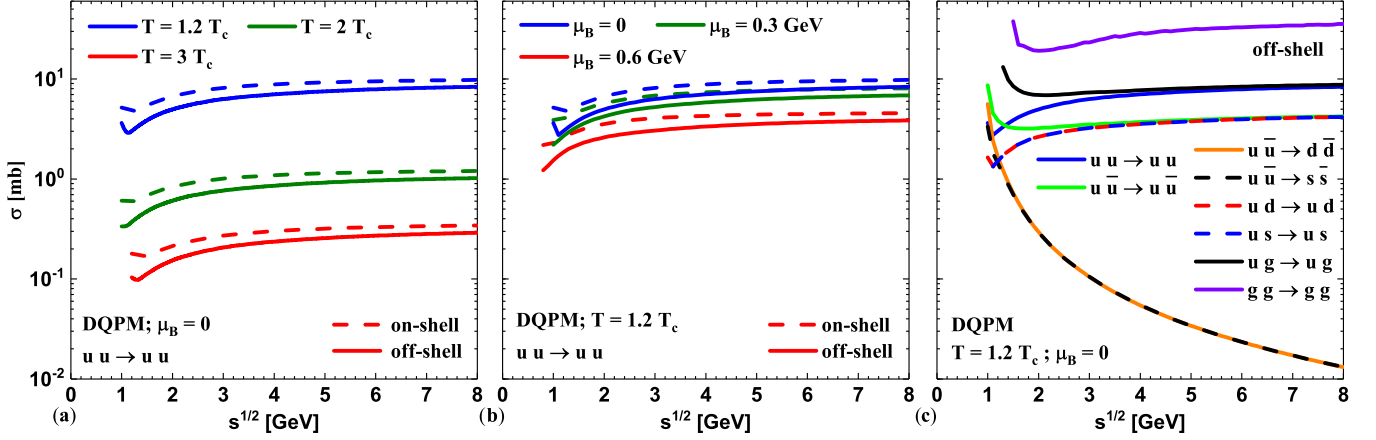
FIG. 5. Cross sections between different partons for the on-shell case (dashed lines) from Eq. (20) and the off-shell case (solid lines) from Eq. (24) evaluated in the center of mass of the collision system as a function of the collision energy $\sqrt{s}$ (see text for a detailed description). The initial masses of the colliding partons are taken as the pole masses from Eqs. (4) and (5).

element (squared) $|\bar{\mathcal{M}}|^2$, entering the differential cross section in Eqs. (17)–(21), is calculated in leading order and is averaged over initial—and summed over final—spin and colors. In the following, we employ a degeneracy factor for spin and color of $d_q = 2 \times N_c = 6$ for quarks and $d_g = 2 \times (N_c^2 - 1) = 16$ for gluons in consistency with Eqs. (11) and (12). Each matrix element can be decomposed into several channels known as $t-$, $u-$, and $s-$channels for quark-quark (qq') and quark-gluon (qg) scatterings, as well as a four-point interaction for the case of gluon-gluon (gg) scattering. For details, we refer the reader to the Appendixes A–C and continue with the actual results.

In Fig. 4, we show the differential cross sections between different partons for the on-shell case (dashed lines) from Eq. (18) and the off-shell case (solid lines) evaluated in the center-of-mass of the collision system as a function of the collision energy $\sqrt{s}$. In these examples, the initial masses of the colliding partons are taken as the pole masses from Eqs. (4) and (5) to allow for a comparison between on-shell and off-shell scattering, i.e., for the same initial states. In all cases [$uu \to uu$ (a), $ud \to ud$ (b), $ug \to ug$ (c), $gg \to gg$ (d)], the cross sections are almost isotropic at the threshold energy $\sqrt{s} \approx 1$ GeV and increase in anisotropy with increasing $\sqrt{s}$. Furthermore, the on-shell case (dashed lines) gives slightly larger cross sections than the off-shell case (solid lines), which will be discussed below.

Figure 5(a) displays the angle integrated cross section for $uu \to uu$ scattering as a function of $\sqrt{s}$ for temperatures of $T = 1.2T_c$ (blue), $T = 2T_c$ (green), and $T = 3T_c$ (red) for the on-shell (dashed lines) and off-shell (solid lines) cases at $\mu_B = 0$. Again, the initial masses of the colliding partons

are taken as the pole masses from Eqs. (4) and (5) to obtain the same initial flux F. At all temperatures T, the cross section does not change very much with collision energy $\sqrt{s}$ and the difference between the on-shell and off-shell case decreases with increasing $\sqrt{s}$. The explicit dependence of the $uu \to uu$ cross section on the chemical potential is shown in Fig. 5(b) for $\mu_B = 0$ (blue), $\mu_B = 0.3$ GeV (green), and $\mu_B = 0.6$ GeV (red) at $T = 1.2T_c$ for the on-shell (dashed lines) and off-shell (solid lines) cases. While the dependencies on $\sqrt{s}$ are similar, we find a decrease of the cross section with increasing chemical potential μ_B which can be traced back to a decreasing coupling with μ_B at fixed temperature T (see Fig. 1). Figure 5(c), furthermore, shows the dependence of all cross sections calculated on the collision energy $\sqrt{s}$ in the off-shell case for $T = 1.2T_c$ and $\mu_B = 0$. While most of the channels do not change drastically with $\sqrt{s}$—except for thresholds—the flavor-changing processes $u\bar{u} \to d\bar{d}$ and $u\bar{u} \to s\bar{s}$ drop quickly with increasing energy.

With all differential partonic cross sections fixed as a function of T and μ_B (above the phase boundary), we can now continue with transport properties of the hot QGP as a function of T and μ_B employing the partonic energy-momentum distributions from the DQPM.

IV. COLLISIONAL WIDTHS OF THE HOT AND DENSE QGP

A. On-shell case

In the on-shell case, all energies of the particles are taken to be $E^2 = \mathbf{p}^2 + M^2$, where M is the pole mass. The on-shell interaction rate for the corresponding parton is given by [34,83,84]

$$
\begin{aligned}
\Gamma_i^{\text{on}}(\mathbf{p}_i, T, \mu_q) &= \frac{1}{2E_i} \sum_{j=q,\bar{q},g} \int \frac{d^3 p_j}{(2\pi)^3 2E_j} d_j f_j(E_j, T, \mu_q) \int \frac{d^3 p_3}{(2\pi)^3 2E_3} \int \frac{d^3 p_4}{(2\pi)^3 2E_4} (1 \pm f_3)(1 \pm f_4) \\
&\quad \times |\bar{\mathcal{M}}|^2(p_i, p_j, p_3, p_4)\, (2\pi)^4 \delta^{(4)}(p_i + p_j - p_3 - p_4) \\
&= \sum_{j=q,\bar{q},g} \int \frac{d^3 p_j}{(2\pi)^3} d_j f_j v_{\text{rel}} \int d\sigma_{ij \to 34}^{\text{on}} (1 \pm f_3)(1 \pm f_4),
\end{aligned}
\tag{29}
$$

where d_j is the degeneracy factor for spin and color [for quarks $d_q = 2 \times N_c$ and for gluons $d_g = 2 \times (N_c^2 - 1)$], and with the shorthand notation $f_j = f_j(E_j, T, \mu_q)$ for the distribution functions. In Eq. (29) and throughout this section, the notation $\sum_{j=q,\bar{q},g}$ includes the contribution from all possible partons, which in our case are the gluons and the (anti)quarks of three different flavors (u, d, s). The Pauli-blocking $(-)$ and Bose-enhancement $(+)$ factors account for the available density of final states. Note that here all quantities have to be expressed in the rest frame of the heat bath, implying that the on-shell cross section $d\sigma^{\text{on}}$ from Eq. (18) has to be modified according to the different fluxes:

$$F^{\text{HB}} \sigma^{\text{HB}} = \sigma^{\text{c.m.}} F^{\text{c.m.}}, \tag{30}$$

where the quantities denoted by HB are expressed in the rest frame of the heat bath and c.m. in the center-of-mass frame of the collision.

To evaluate the average width of the partons i, we finally have to average its interaction rate (29) over its momentum distribution,

$$\Gamma_i^{\text{on}}(T, \mu_q) = \frac{d_i}{n_i^{\text{on}}(T, \mu_q)} \int \frac{d^3 p_i}{(2\pi)^3} f_i(E_i, T, \mu_q) \Gamma_i^{\text{on}}(\mathbf{p}_i, T, \mu_q) \tag{31}$$

with the on-shell density of partons i at T and μ_q given by

$$n_i^{\text{on}}(T, \mu_q) = d_i \int \frac{d^3 p_i}{(2\pi)^3} f_i(E_i, T, \mu_q). \tag{32}$$

B. Off-shell case

In order to obtain the width for the off-shell DQPM timelike partons, we have to calculate the interaction rate for the corresponding parton i with momentum $\mathbf{p}_i$ due to collisions with timelike particles j leading to final timelike particles 3 and 4 by integrating additionally over all energies ω_j in the timelike sector:

$$\Gamma_i^{\text{off}}(\mathbf{p}_i, T, \mu_q) = \int_0^\infty \frac{d\omega_i}{(2\pi)} \tilde{\rho}_i \sum_{j=q,\bar{q},g} \int \frac{d^4 p_j}{(2\pi)^4} \theta(\omega_j) d_j \tilde{\rho}_j f_j \int \frac{d^4 p_3}{(2\pi)^4} \theta(\omega_3) \tilde{\rho}_3 \int \frac{d^4 p_4}{(2\pi)^4} \theta(\omega_4) \tilde{\rho}_4 (1 \pm f_3)(1 \pm f_4)$$

$$\times |\bar{\mathcal{M}}|^2(p_i, p_j, p_3, p_4) (2\pi)^4 \delta^{(4)}(p_i + p_j - p_3 - p_4), \tag{33}$$

where the shorthand notation (22) for the renormalized timelike spectral functions $\tilde{\rho}_j(\omega_j, \mathbf{p}_j)$ has been used and $f_j = f_j(\omega_j, T, \mu_q)$ for the distribution functions. We mention that the limit (33) discards damping processes between the timelike and spacelike sector which are assumed to be subleading. To evaluate the average timelike width of the partons i, we finally have to average its interaction rate as

$$\Gamma_i^{\text{off}}(T, \mu_q) = \frac{d_i}{n_i^{\text{off}}(T, \mu_q)} \int \frac{d^4 p_i}{(2\pi)^4} \theta(\omega_i) \tilde{\rho}_i f_i(\omega_i, T, \mu_q) \sum_{j=q,\bar{q},g} \int \frac{d^4 p_j}{(2\pi)^4} \theta(\omega_j) d_j \tilde{\rho}_j f_j \int \frac{d^4 p_3}{(2\pi)^4} \theta(\omega_3) \tilde{\rho}_3$$

$$\times \int \frac{d^4 p_4}{(2\pi)^4} \theta(\omega_4) \tilde{\rho}_4 (1 \pm f_3)(1 \pm f_4) |\bar{\mathcal{M}}|^2(p_i, p_j, p_3, p_4) (2\pi)^4 \delta^{(4)}(p_i + p_j - p_3 - p_4), \tag{34}$$
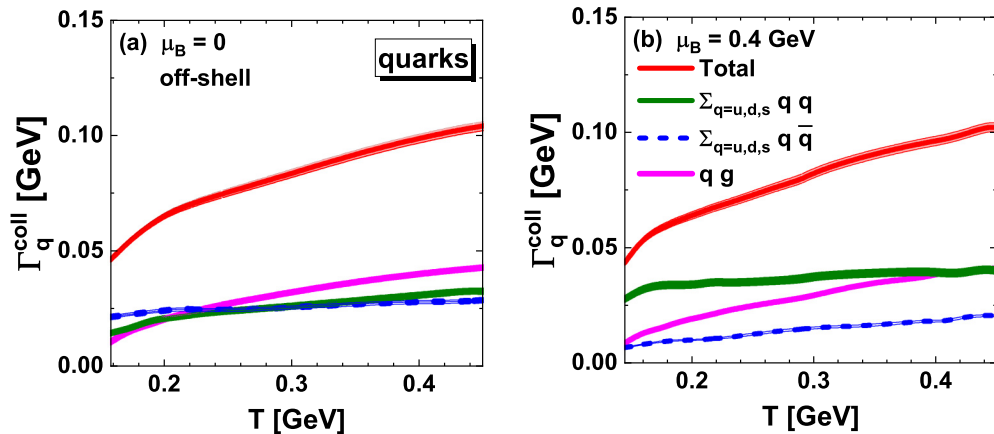
FIG. 6. Off-shell collision rate from Eq. (34) of a light quark q as a function of the temperature T for $\mu_B = 0$ (a) and $\mu_B = 0.4$ GeV (b) (blue lines). The contributions from the scattering with light quarks (green), antiquarks (blue), and gluons (pink) are given by the lower hatched bands which arise from the finite statistics in the evaluation of the integrals by Monte Carlo.
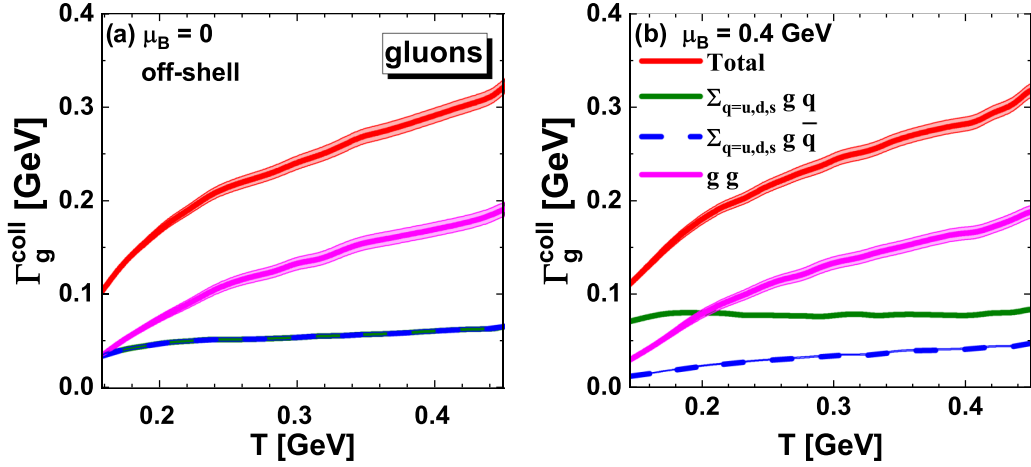
FIG. 7. Off-shell collision rate from Eq. (34) of a gluon g as a function of the temperature T for $\mu_B = 0$ (a) and $\mu_B = 0.4$ GeV (b). The contributions from the scattering with light quarks (green), antiquarks (blue), and gluons (pink) are given by the lower hatched bands which arise from the finite statistics in the evaluation of the integrals by Monte Carlo.

with the off-shell density of timelike partons i given by

$$n_i^{\mathrm{off}}(T, \mu_q) = d_i \int \frac{d^4 p_i}{(2\pi)^4} \, \theta(\omega_i) \, 2\omega_i \, \tilde{\rho}_i \, f_i(T, \mu_q). \quad (35)$$

Figure 6 shows the "off-shell interaction rate" Γ_q^{coll} of a light quark q as a function of the temperature T for $\mu_B = 0$ (a) and $\mu_B = 0.4$ GeV (b). The contributions from the scattering with light quarks (green), antiquarks (blue), and gluons (pink) are given by the lower hatched bands. At $\mu_B = 0$, the total width Γ_q^{coll} to a large extend stems from quark-gluon scattering and increases with temperature while the contributions from scatterings with quarks and antiquarks are about equal and subdominant. At $\mu_B = 0.4$ GeV, the quarks are more abundant than the antiquarks and the contributions from scatterings with quarks increase while that from collisions with antiquarks decrease relative to $\mu_B = 0$. The contributions from collisions with gluons slightly decreases also with μ_B,

which can be attributed to a decrease of the cross sections with μ_B as noted before. Figure 7 shows the off-shell interaction rate of a gluon g as a function of the temperature T for $\mu_B = 0$ (a) and $\mu_B = 0.4$ GeV (b) as in case of quark scattering in Fig. 6. The contributions from the scattering with light quarks (green), antiquarks (blue), and gluons (pink) are given by the lower hatched bands. The discussion of the contributions to the total widths is very similar to the case of quark scattering and not repeated here.

In summarizing this section, we find that the collisional widths for timelike partons are sizable and increase with temperature (as in the DQPM) but still remain substantially smaller than the pole masses in Fig. 2. Accordingly, a quasi-particle interpretation for timelike quanta should approximately hold.

Figure 8, finally, gives an overview on the width Γ_q (a) and width Γ_g (b) as a function of the scaled temperature
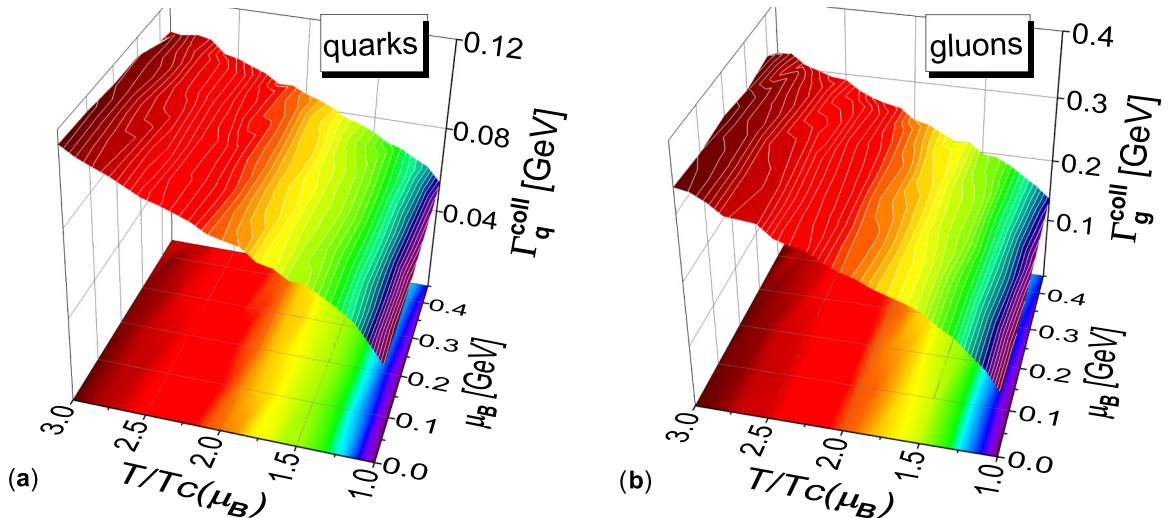
FIG. 8. Off-shell collision rate of a quark (a) and gluon (b) as a function of the scaled temperature $T/T_c(\mu_B)$ and the baryon chemical potential μ_B from Eq. (34).

$T/T_c(\mu_B)$ and chemical potential μ_B. While the dependencies on temperature are similar for fixed μ_B, we see a general slight decrease of the total widths with μ_B for fixed $T/T_c(\mu_B)$ as discussed above.

V. TRANSPORT PROPERTIES OF THE HOT AND DENSE QGP

The starting point to evaluate viscosity coefficients of partonic matter is the Kubo formalism [85–92], which was used to calculate the viscosities for a previous version of the DQPM within the PHSD in a box with periodic boundary conditions (cf. Ref. [93]). We focus here on the calculation of the shear viscosity based on Refs. [87–90], which reads

$$
\eta^{\text{Kubo}}(T, \mu_q) = -\int \frac{d^4 p}{(2\pi)^4} \, p_x^2 p_y^2 \sum_{i=q,\bar{q},g} d_i \, \frac{\partial f_i(\omega)}{\partial \omega} \, \rho_i(\omega, \mathbf{p})^2
$$

$$
= \frac{1}{15T} \int \frac{d^4 p}{(2\pi)^4} \, \mathbf{p}^4 \sum_{i=q,\bar{q},g}
$$

$$
\times \, d_i((1 \pm f_i(\omega))f_i(\omega))\rho_i(\omega, \mathbf{p})^2, \quad (36)
$$

where the notation $f_i(\omega) = f_i(\omega, T, \mu_q)$ is used for the distribution functions, and ρ_i denotes the spectral functions from Eq. (8). We note that the derivative of the distribution function accounts for the Pauli-blocking $(-)$ and Bose-enhancement $(+)$ factors. Following Ref. [89], we can evaluate the integral over $\omega = p_0$ in Eq. (36) by using the residue theorem. When keeping only the leading-order contribution in the width $\gamma(T, \mu_B)$ from the residue—evaluated at the poles of the spectral function $\omega_i = \pm \tilde{E}(\mathbf{p}) \pm i\gamma$—we finally obtain

$$
\eta^{\text{RTA}}(T, \mu_q) = \frac{1}{15T} \int \frac{d^3 p}{(2\pi)^3} \sum_{i=q,\bar{q},g}
$$

$$
\times \left(\frac{\mathbf{p}^4}{E_i^2 \, \Gamma_i(\mathbf{p}_i, T, \mu_q)} \, d_i((1 \pm f_i(E_i))f_i(E_i)) \right)
$$

$$
+ O(\Gamma_i), \quad (37)
$$

which corresponds to the expression derived in the relaxation-time approximation (RTA) [94–98] by identifying the interaction rate Γ with 2γ as expected from transport theory in the quasiparticle limit [21]. This interaction rate $\Gamma_i(\mathbf{p}_i, T, \mu_q)$ (inverse relaxation time) is calculated microscopically by Eq. (29). We recall that the pole energy is $E_i^2 = p^2 + M_i^2$, where M_i is the pole mass given in the DQPM by Eqs. (4) and (5). As in the previous section, we use here the notation $\sum_{j=q,\bar{q},g}$, which includes the contribution from all possible partons which in our case are the gluons and the (anti)quarks of three different flavors (u, d, s).

The actual results are displayed in Fig. 9 for the ratios of shear viscosity to entropy density η/s as a function of the scaled temperature T/T_c for $\mu_B = 0$ in comparison to those from lattice QCD [101]. The solid green line (η^{Kubo}/s) shows the result from the original DQPM in the Kubo formalism while the dashed green line ($\eta_{2\gamma}^{\text{RTA}}/s$) shows the same result in the quasiparticle approximation (37) by replacing Γ_i by $2\gamma_i$. The solid red line ($\eta_{\Gamma^{\text{on}}}^{\text{RTA}}/s$) results from Eq. (37) using the interaction rate Γ^{on} (29) calculated by the microscopic
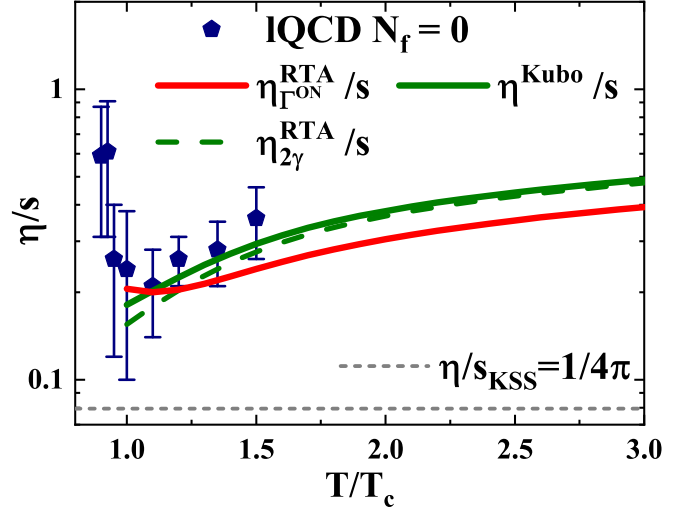
FIG. 9. The ratio of shear viscosity to entropy density as a function of the scaled temperature T/T_c for $\mu_B = 0$ from Eqs. (36) and (37). The solid green line (η^{Kubo}/s) shows the results from the original DQPM in the Kubo formalism while the dashed green line ($\eta_{2\gamma}^{\text{RTA}}/s$) shows the same result in the quasiparticle approximation (37). The solid red line ($\eta_{\Gamma^{\text{on}}}^{\text{RTA}}/s$) results from Eq. (37) using the interaction rate Γ^{on} (29) calculated by the microscopic differential cross sections in the on-shell limit. The dashed gray line demonstrates the Kovtun-Son-Starinets bound [99,100] $(\eta/s)_{\text{KSS}} = 1/(4\pi)$, and the symbols show lQCD data for pure SU(3) gauge theory taken from Ref. [101] (pentagons).

differential cross sections in the on-shell limit. We find that—apart from temperatures close to T_c—the ratios η/s do not differ very much and have a similar behavior as a function of temperature. The approximation (37) of the shear viscosity is found to be very close to the one from the Kubo formalism (36), indicating that the quasiparticle limit ($\gamma \ll M$) holds in the DQPM. We have also checked that the shear viscosity does not differ substantially if one uses the momentum-dependent interaction rate from Eq. (29) or the averaged one from Eq. (31).

An overview for the ratio of shear viscosity to entropy density η/s as a function of the scaled temperature $T/T_c(\mu_B)$ and μ_B is given in Fig. 10 in case of the Kubo formalism (a) (36) and the on-shell limit (37) (b). There is no strong variation with μ_B for fixed $T/T_c(\mu_B)$; however, the ratio increases slightly with μ_B in the on-shell limit while it slightly drops with μ_B in the Kubo formalism for the DQPM. Accordingly, there is some model uncertainty when extracting the shear viscosity in the different approximations.

In summarizing this section, we find that the results for the ratio of shear viscosity over entropy density from the original DQPM and those from the microscopic calculations are similar and within error bars compatible with present results from lattice QCD. However, having the differential cross sections for each partonic channel at hand one might find substantial differences for nonequilibrium configurations as encountered in relativistic heavy-ion collisions where a QGP is formed initially out of equilibrium.
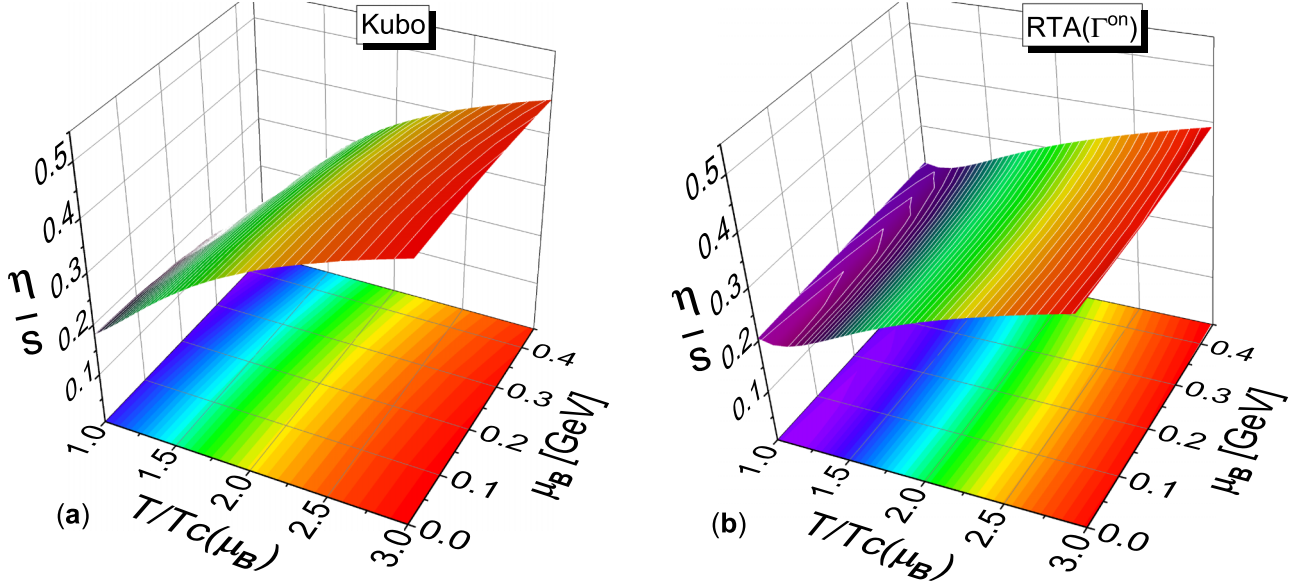
FIG. 10. The ratio of shear viscosity to entropy density η/s as a function of the scaled temperature $T/T_c(\mu_B)$ and baryon chemical potential μ_B calculated within the Kubo formalism (a) from Eq. (36) and in the relaxation-time approximation (RTA) (b) from Eq. (37) using the on-shell interaction rate Γ^{on} from Eq. (29).

VI. EXTRACTION OF T AND μ_B FROM PHSD IN HEAVY-ION COLLISIONS

Since PHSD is a microscopic off-shell transport approach, it does not incorporate thermodynamic Lagrange parameters such as T and μ_B that characterize the system in equilibrium. In order to extract the required information (the temperature T and baryon chemical potential μ_B)—defining the parton properties and differential scattering processes in the PHSD space-time grid—we use a parametrization of the lQCD equation of state from Ref. [102] where the pressure (negative thermodynamic potential) is expanded as

$$\frac{P}{T^4} = c_0(T) + c_2(T)\left(\frac{\mu_B}{T}\right)^2 + c_4(T)\left(\frac{\mu_B}{T}\right)^4 + O(\mu_B^6).$$
(38)

This equation of state matches the conditions of a heavy-ion collision where strangeness neutrality $\langle n_S \rangle = 0$ is realized on average and where the relation between electric charge and baryon number $\langle n_Q \rangle = 0.4 \langle n_B \rangle$ is fixed by the content of the initial nuclei. We mention that the inclusion of the sixth-order coefficient c_6 induces wiggles in the EoS due to oscillating contributions in Eq. (38) (see also Ref. [75]) but does not lead to considerable changes for $\mu_B/T < 3$ and is discarded here. Note that the parametrization of the coefficients $c_i(T)$ in Eq. (38) is also in agreement with lQCD data below T_c which allows for an evaluation of T and μ_B also in the hot hadronic phase. We point out that these results have to be taken as estimates in the regions of large chemical potentials for $\mu_B/T > 3$.

In each space-time cell of the PHSD grid, the thermodynamic quantities are calculated by the method developed in Ref. [103], i.e., by diagonalization of the energy momentum tensor $T^{\mu\nu}$ as

$$T^{\mu\nu}(x_\nu)_i = \lambda_i(x^\mu)_i = \lambda_i\, g^{\mu\nu}(x_\nu)_i,$$
(39)

with $i = 0, 1, 2, 3$, where λ_i are the eigenvalues of $T^{\mu\nu}$ and $(x_\nu)_i$ are the corresponding eigenvectors. For $i = 0$, the local energy density ϵ is identified with the eigenvalue of $T^{\mu\nu}$ (Landau matching) and the corresponding timelike eigenvector is defined as the 4-velocity u_ν:

$$T^{\mu\nu}u_\nu = \epsilon u^\mu = (\epsilon g^{\mu\nu})u_\nu$$
(40)

using the normalization condition $u^\mu u_\mu = 1$. The three other solutions are $(-P_i)$, the pressure components expressed in the local rest frame of the cell. The energy-momentum tensor $T^{\mu\nu}$ is calculated in PHSD as

$$T^{\mu\nu} = \sum_i \frac{p_i^\mu p_i^\nu}{E_i},$$
(41)

where the sum i runs over all the particles in the considered cell.

To study the matter at finite baryon density, we calculate additionally the net-baryon current

$$J_B^\mu = \sum_i \frac{p_i^\mu}{E_i} \frac{(q_i - \bar{q}_i)}{3},$$
(42)

with q_i $(\bar{q}_i)$ being the number of light quarks (antiquarks) within particle i. To obtain the local net-baryon density, we apply the Lorentz transformation defined via

$$n_B = \gamma_E\left(J_B^0 - \vec{\beta}_E \cdot \vec{J}_B\right) = \frac{J_B^0}{\gamma_E},$$
(43)

where $\vec{\beta}_E = \vec{J}_B / J_B^0$ is known as the Eckart velocity and γ_E is the associated Lorentz factor. We mention that by using the Eckart velocity $\vec{\beta}_E$ to transform the net-baryon current, the
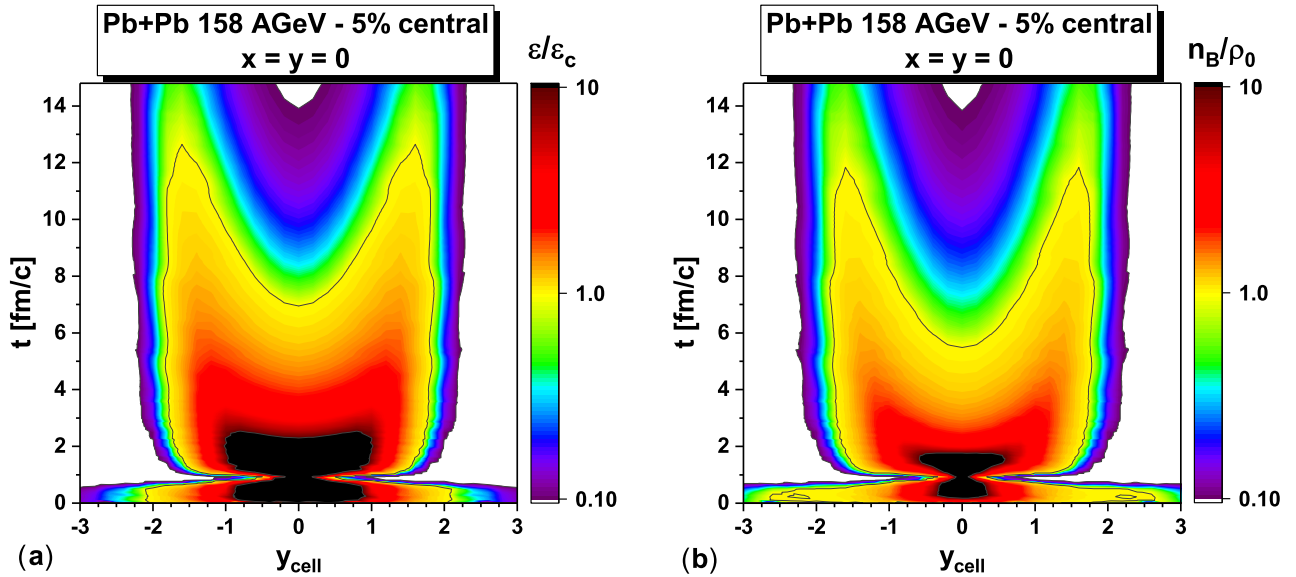
FIG. 11. The energy density ϵ (left) and baryon density n_B (right) as a function of the cell rapidity y_{cell} at different times t for 5% central Pb+Pb collisions at 158 A GeV extracted from the central cell $x = y = 0$ of the PHSD. The energy density and baryon density are divided by the critical energy density $\epsilon_c = 0.5\,\text{GeV/fm}^3$ and the saturation density $\rho_0 = 0.17\,\text{fm}^{-3}$, respectively. The initial time $t = 0$ is systematically taken to be the time of the first nucleon-nucleon collision.

spatial part of the latter automatically vanishes, whereas this is not guaranteed when employing the energy flow u^μ from Eq. (40).

We illustrate in Fig. 11 our extraction method and show the time and rapidity dependence of the energy density ϵ and baryon density n_B extracted from the PHSD in the central cell $x = y = 0$ of 5% central Pb + Pb collisions at 158 A GeV. We mention that in the PHSD the parallel ensemble method is used, implying that the densities are averaged over a large number of parallel events ($\approx$250 for AGS energies, $\approx$150 for top SPS, and $\approx$30 for top RHIC). With this procedure, even if each event contains only a few particles per cell, the overall profile is relatively smooth in space-time. Furthermore, in the evaluation of the energy density ϵ and baryon density n_B, leading quarks or diquarks are also included since they carry most of the baryon number in the string fragmentation picture. The cell rapidity y_{cell} is evaluated from the cell 4-velocity $u^\mu = \gamma(1, \vec{\beta})$ in Eq. (40) as $y_{\text{cell}} = 1/2\log[(1 + \beta_z)/(1 - \beta_z)]$. For illustration, we have scaled the energy and baryon densities by the critical energy density $\epsilon_c = 0.5\,\text{GeV/fm}^3$ used in the PHSD and the saturation density $\rho_0 = 0.17\,\text{fm}^{-3}$, respectively. One can see that at the collision time ($t = 0$) a high amount of energy is deposited into the midrapidity region whereas at higher rapidities the initial nuclei are still intact. Indeed, we observe that around the initial rapidity of the nuclei ($y_N \approx 2.9$) the baryon density is still close to the saturation density ρ_0. After the passing time $t = R/\gamma_N \approx 0.75$ fm/c, all the initial nucleons in the central cell ($x = y = 0$) have interacted and maximal values for the energy density and baryon density are reached which are of the order of $\epsilon \approx 5\,\text{GeV/fm}^3$ and $n_B \approx 2\,\text{fm}^{-3}$, respectively. We can identify approximatively constant values of ϵ and n_B as a function of the cell rapidity y_{cell} along parabolas of proper

time $\tau \sim t/\cosh(y_{\text{cell}})$. After $\tau \approx 6$ fm/c, the energy density reaches the critical value ϵ_c, implying that quarks and gluons hadronize into hadrons, whereas the baryon density appears to be slightly lower than the saturation density ρ_0.

In the beginning of heavy-ion collisions, the created medium is highly anisotropic due to the longitudinal expansion. In order to correct for the anisotropy, we apply the *shape generalized equation of state* developed in Ref. [104] in order to extract values for the temperature T and baryon chemical potential μ_B. In this framework, the energy density ϵ^{anis} and pressure components of an anisotropic medium are evaluated by the following expressions:

$$\epsilon^{\text{anis}} = \epsilon^{\text{EoS}} \, r(x), \tag{44}$$

$$P_\perp = P^{\text{EoS}} [r(x) + 3xr'(x)], \tag{45}$$

$$P_\parallel = P^{\text{EoS}} [r(x) - 6xr'(x)], \tag{46}$$

where $P_\perp$ and $P_\parallel$ are, respectively, the transverse and longitudinal pressures, and ϵ^{EoS} and P^{EoS} are the equilibrium energy density and pressure from which a temperature T and chemical potential μ_B can be extracted. The anisotropy parameter x can be approximated as a function of the pressure components as $P_\parallel/P_\perp = x^{-3/4}$, and the function $r(x)$ reads

$$r(x) = \begin{cases} \frac{x^{-1/3}}{2}\left[1 + \frac{x\,\text{arctanh}\sqrt{1-x}}{\sqrt{1-x}}\right] & \text{for } x \leqslant 1 \\ \frac{x^{-1/3}}{2}\left[1 + \frac{x\arctan\sqrt{x-1}}{\sqrt{x-1}}\right] & \text{for } x \geqslant 1. \end{cases} \tag{47}$$

In a PHSD simulation, we calculate in each of the cells the energy density ϵ^{PHSD}, the baryon density n_B^{PHSD}, as well as the pressure components $P_\perp^{\text{PHSD}}$ and $P_\parallel^{\text{PHSD}}$, from which one can evaluate the function $r(x)$ in Eq. (47). In order to find the temperature T and baryon chemical potential μ_B according to the EoS—constructed at the beginning of this section—we
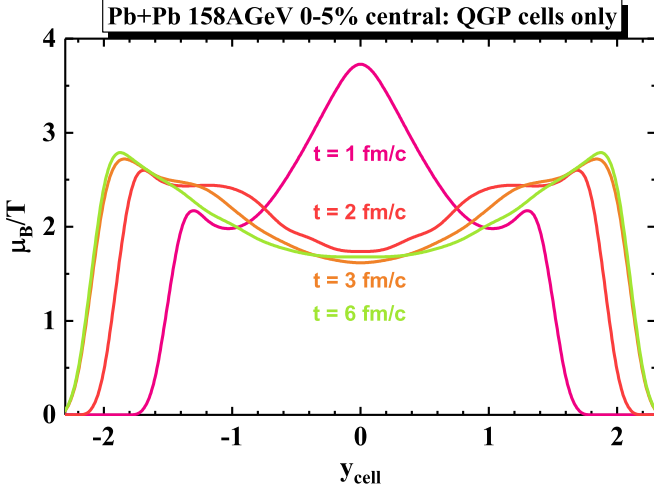
FIG. 12. The ratio μ_B/T as a function of the cell rapidity y_{cell} at different times t for 5% central Pb + Pb collisions at 158 A GeV from PHSD.

FIG. 13. The temperature profile (for the central cell) as a function of the cell rapidity y_{cell} and different times (from 0.15 to 7 fm/c) for a 5% central Au + Au collision at $\sqrt{s_{NN}} = 200$ GeV from PHSD. The dashed lines result when extracting the temperature directly from the energy density of the central cell in PHSD ϵ^{PHSD} while the solid lines refer to the extraction from the equation of state ϵ^{EoS} (see text).

have to solve the following system of equations:

$$\epsilon^{EoS}(T, \mu_B) = \epsilon^{PHSD}/r(x)$$
$$n_B^{EoS}(T, \mu_B) = n_B^{PHSD}, \qquad (48)$$

where the left-hand sides represent the EoS which depends on the unknowns T and μ_B, whereas on the right-hand sides of these equations we have the energy density and baryon density evaluated in PHSD. In Eq. (48), the energy density from PHSD ϵ^{PHSD} is divided by the function $r(x)$ from Eq. (47) to account for the anisotropy of the considered cell according to the *shape generalized equation of state* in Eq. (44). We solve this system by using the Newton-Raphson method [105,106].

We now turn to the evaluation of T and μ_B in actual PHSD simulations for A + A collisions. As an example for our results, we show in Fig. 12 the ratio μ_B/T as a function of the cell rapidity y_{cell} at different times (from 1 to 6 fm/c) for 5% central Pb + Pb collisions at 158 A GeV. The largest ratios are seen for all times for rapidities closer to projectile and target rapidities (cf. Ref. [55]), while at midrapidity this ratio is initially high (at $t = 1$ fm/c) but drops to $\mu_B/T \sim 2$ at $t = 2$ fm/c and remains approximately constant afterward. We mention that this profile is very close to that calculated in the hydrodynamics + hadronic transport approach by Denicol *et al.* (Fig. 5 in Ref. [52]) and also shows an increase of μ_B/T with increasing $|y|$.

Figure 13 shows the temperature profile (for the central cell) as a function of the cell rapidity y_{cell} and different times (from 0.15 to 7 fm/c) for a 5% central Au + Au collision at $\sqrt{s_{NN}} = 200$ GeV. This temperature profile initially ($t = 0.15$ fm/c) has a broad maximum at midrapidity but for $t > 0.25$ fm/c slight maxima at $|y_{cell}| \approx 1.5$ appear which move to higher cell rapidity with increasing time while the average temperature drops rapidly in time. The lowest temperatures (at midrapidity), however, are still on the level of 250 MeV at $t = 2$ fm/c, i.e., well above the critical temperature T_c. We note in passing that the temperature profiles from two different extraction methods, directly from the energy

density of the cell in PHSD ϵ^{PHSD} (dashed lines)—setting $r(x) = 1$ in Eq. (48)—and from the equation of state ϵ^{EoS} (solid lines) are practically the same for $t \geqslant 0.25$ fm/c and provide an idea about the accuracy of our extraction method.

We now focus on the space-time distribution of the extracted temperatures T (left column) and chemical potentials μ_B (right column) for a 5% central collision of Pb + Pb at 158 A GeV from PHSD as shown in Fig. 14. These distributions correspond to the transverse plane (x, y)—orthogonal to the beam direction—at midrapidity ($|y_{cell}| < 1$), i.e., in the center of the collision zone. For early times, we find the temperatures of the fireball to be well above T_c practically everywhere, with a maximum in the center. Then the fireball expands in space with time while the temperature (and thus the QGP region) drops accordingly. Indeed, at $t = 4$ fm/c the temperature is above T_c only in the very central region, whereas on the outside hadronization already occurred. This is in line with the common picture of fireball expansion and hadronization. However, the profile in the chemical potential μ_B (right column) shows that the chemical potential μ_B is very large for early times in the whole fireball and drops to values of around ≈ 0.2–0.3 in the hot QGP zone for $t \approx 4$ fm/c.

We close this section by visualizing the time evolution of the distribution in T and μ_B for cells having a temperature $T > T_c(\mu_B)$ at midrapidity ($|y_{cell}| < 1$) for 5% central heavy-ion collisions. Figure 15(a) shows this distribution for a Au + Au collision at $\sqrt{s_{NN}} = 200$ GeV from PHSD for times $t < 0.5$ fm/c, 0.5 fm/c $< t < 2$ fm/c, and $t > 2$ fm/c. The scale corresponds to the number of cells in the PHSD event in the considered bin in $T - \mu_B$ divided by the total number of cells in the corresponding time window while the solid black line is the DQPM phase boundary for orientation. At
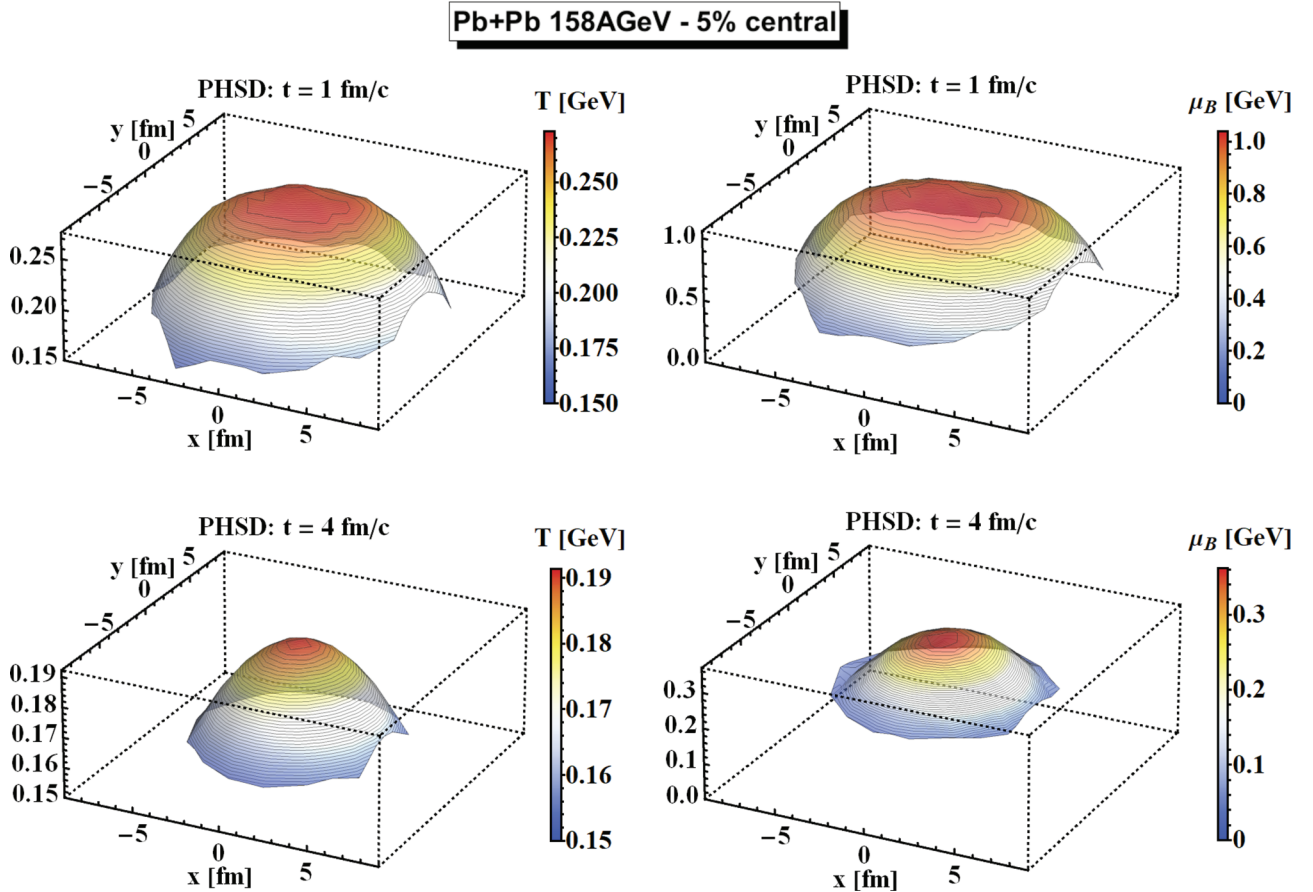
FIG. 14. (Left) The temperature profile in (x, y) at midrapidity ($|y_{\mathrm{cell}}| < 1$) at 1 and 4 fm/c after the initial collision in case of a 5% central Pb + Pb collision at 158 A GeV from PHSD. (Right) The profile in the chemical potential μ_B in (x, y) at midrapidity ($|y_{\mathrm{cell}}| < 1$) for different times from 0.5 to 6 fm/c for the same collision.

the very early times $t < 0.5$ fm/c, the distribution peaks at $T \approx 0.3$ GeV and is concentrated around $\mu_B \approx 0$. For times 0.5 fm/c $< t < 2$ fm/c, the average temperature has dropped to about 0.24 GeV, and for later times ($t > 2$ fm/c), the distribution peaks at an average temperature slightly above T_c. Note that a negative μ_B implies that there are more antiquarks (antibaryons) than quarks (baryons) in the individual cell. This time evolution of the distribution at the top RHIC energy matches well-known expectations.

Figure 15(b) shows the distribution in T and μ_B for cells at midrapidity ($|y_{\mathrm{cell}}| < 1$) in case of Pb + Pb collisions at 158 A GeV from PHSD for times $t < 2$ fm/c, 2 fm/c $< t < 4$ fm/c, and $t > 4$ fm/c. For early times $t < 2$ fm/c, the distribution peaks at a temperature of about 0.25 GeV and a sizable chemical potential of about 0.6 GeV, while for times in the interval 2 fm/c $< t < 4$ fm/c, the maximum has dropped already to an average temperature ≈ 0.18 GeV and a chemical potential of about 0.3 GeV. For later times $t > 4$ fm/c, the distribution (above T_c) essentially stays around $\mu_B \approx 0.25$ GeV. We mention that the values of μ_B probed around the transition temperature T_c in the PHSD are in accordance with the expectation from statistical models which for central Pb + Pb collisions at 158 A GeV quote a value of $\mu_B = 0.2489$ GeV [107]. Furthermore, the trajectory of the fireball in the (T, μ_B) plane resembles the isentropic

trajectories shown in Ref. [102], which for this energy corresponds approximately to a fixed ratio of entropy over baryon density of $s/n_B \approx 40$ [108] and a fixed ratio of $\mu_B/T \approx 2$ (see Fig. 12).

VII. OBSERVABLES FROM RELATIVISTIC NUCLEUS-NUCLEUS COLLISIONS

As mentioned above, the PHSD transport approach [56,60] is a microscopic covariant dynamical model for strongly interacting systems formulated on the basis of Kadanoff-Baym equations [26] for Green's functions in phase-space representation (in first-order gradient expansion beyond the quasiparticle approximation). The approach consistently describes the full evolution of a relativistic heavy-ion collision from the initial hard scatterings and string formation through the dynamical deconfinement phase transition to the strongly interacting quark-gluon plasma (sQGP) as well as hadronization and the subsequent interactions in the expanding hadronic phase as in the hadron-string-dynamics (HSD) transport approach [109]. Note that at lower bombarding energies—without any partonic phase—the PHSD approach merges to the HSD approach with only hadronic and string degrees of freedom. Since we only look for modifications in the partonic sector—cf. Secs. III and IV—we do not further specify the
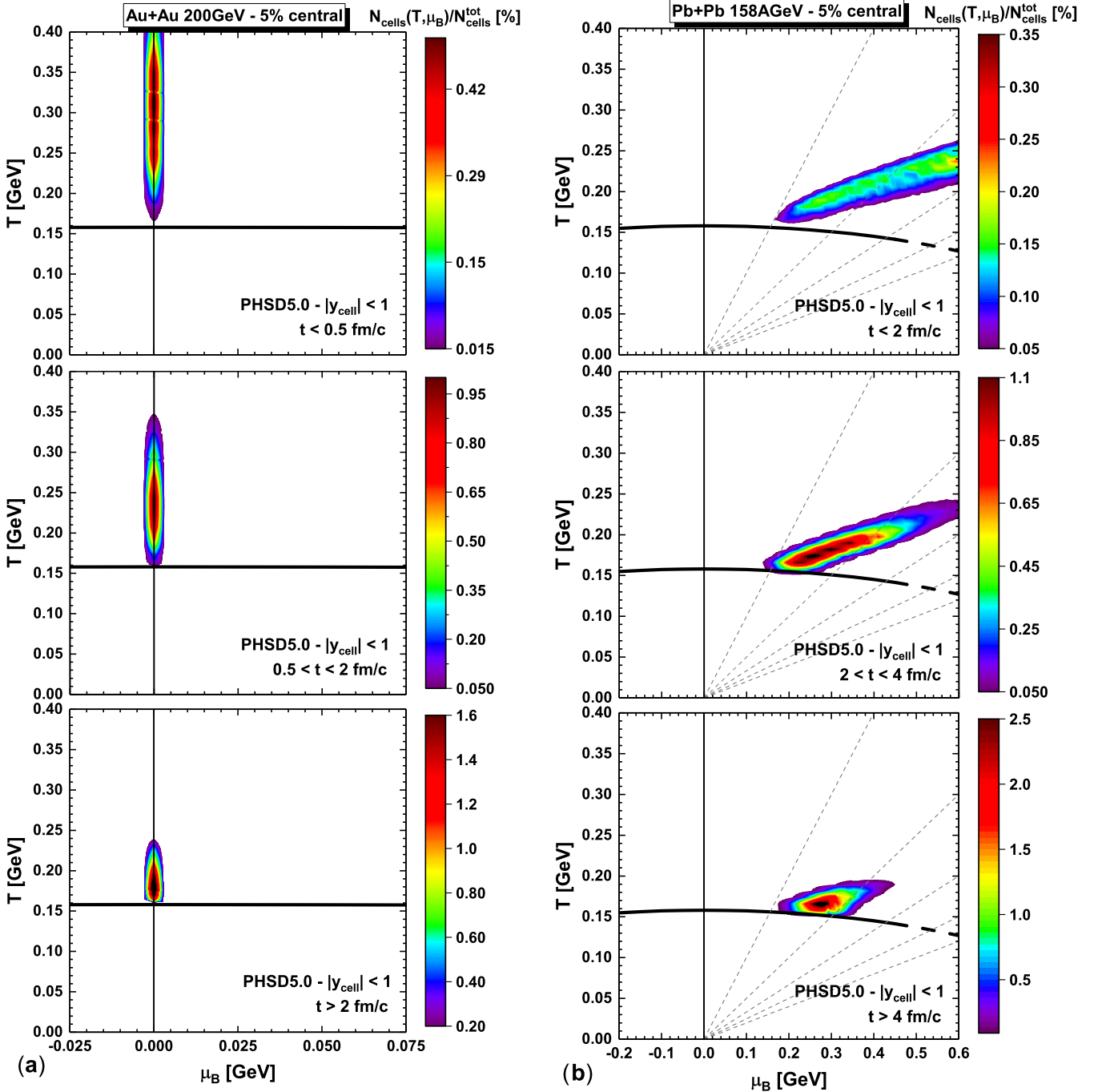
FIG. 15. Distributions in T and μ_B as extracted from the DQPM equation of state in a PHSD simulation of a central Au + Au collision at $\sqrt{s_{NN}} = 200$ GeV (a) and of a central Pb + Pb collision at 158 A GeV (b) for cells with a temperature $T > T_c(\mu_B)$. The scale corresponds to the number of cells in the PHSD event in the considered bin in $T − \mu_B$ divided by the total number of cells in the corresponding time window (see legend). The solid black line is the DQPM phase boundary for orientation, the gray dashed lines indicate ratios of μ_B/T ranging from 1 to 5, while the vertical line stands for $\mu_B = 0$.

hadronic sector and refer the reader to Refs. [46,47,109] for details. We recall that in the PHSD4.0 version, the partonic cross sections are parametrized as a function of the energy density to comply with the individual widths of quarks, anti-quarks, and gluons (cf. Ref. [58]), while the parton masses are parametrized as a function of the scalar density (cf. Ref. [60]).

A. AGS-SPS energies

We start with lower and intermediate energies covered experimentally by the AGS (BNL) and SPS (CERN) with a focus on central Au + Au or Pb + Pb collisions. We will compare results for the "bulk" observables (rapidity distributions and p_T or m_T spectra) from PHSD calculations based on the
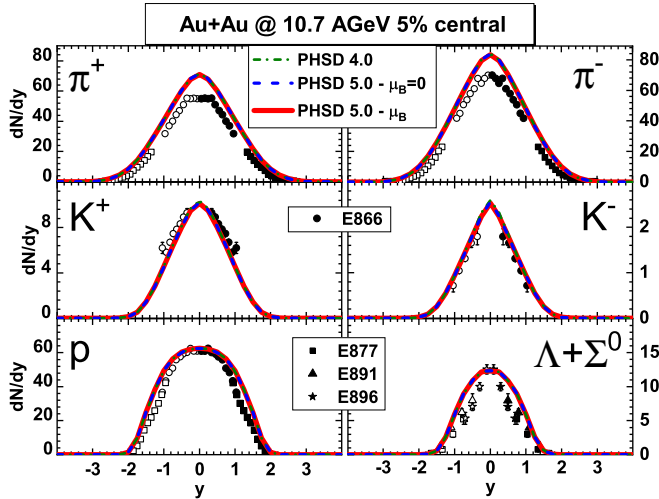
FIG. 16. The rapidity distributions for 5% central Au + Au collisions at 10.7 A GeV for PHSD4.0 (green dot-dashed lines), PHSD5.0 with partonic cross sections and parton masses calculated for $\mu_B = 0$ (blue dashed lines), and with cross sections and parton masses evaluated at the actual chemical potential μ_B in each individual space-time cell (red lines) in comparison to the experimental data from the E866 [110], E877 [111], E891 [112], E877 [113], and E896 [114] Collaborations. All PHSD results are the same within the linewidth.

FIG. 17. The rapidity distributions for 5% central Pb + Pb collisions at 30 A GeV for PHSD4.0 (green dot-dashed lines), PHSD5.0 with partonic cross sections and parton masses calculated for $\mu_B = 0$ (blue dashed lines) and with cross sections and parton masses evaluated at the actual chemical potential μ_B in each individual space-time cell (red lines) in comparison to the experimental data from the NA49 Collaboration [115–117]. All PHSD results are practically the same within the linewidth.

default DQPM parameters (PHSD4.0) with the new PHSD5.0 including the differential cross sections from Sec. III for the individual partonic channels at finite T and μ_B as well as the parton masses $M_i(T, \mu_B)$ from Eqs. (4) and (5). A comparison to the available experimental data is included (for orientation) but not discussed explicitly since this has been done in earlier work in detail [46,47,57].

Figure 16 displays the actual results for hadronic rapidity distributions in the case of 5% central Au + Au collisions at 10.7 A GeV for PHSD4.0 (green dot-dashed lines), PHSD5.0 with partonic cross sections and parton masses calculated for $\mu_B = 0$ (blue dashed lines), and with cross sections and parton masses evaluated at the actual chemical potential μ_B in each individual space-time cell (red lines) in comparison to the experimental data from the E866 [110], E877 [111], E891 [112], E877 [113], and E896 [114] Collaborations. Here, we focus on the most abundant hadrons, i.e., pions, kaons, protons, and neutral hyperons. We note in passing that the effects of chiral symmetry restoration are incorporated as in Refs. [46,47] since this was found to be mandatory to achieve a reasonable description of the strangeness degrees of freedom reflected in the kaon and neutral hyperon dynamics. As seen from Fig. 16, there is no difference in rapidity distributions for all the hadron species from the different versions of PHSD within linewidth, which implies that there is no sensitivity to the new partonic differential cross sections and parton masses employed. One could argue that this result might be due to the low amount of QGP produced at this energy, but the different PHSD calculations for 5% central Pb + Pb collisions at 30 A GeV in Fig. 17 for the hadronic rapidity distributions do not provide a different picture. Only when stepping up to the top
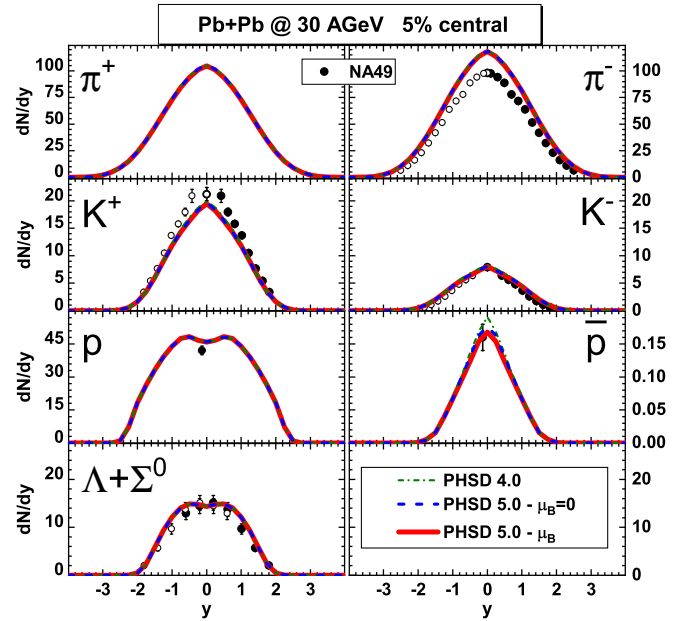
SPS energy of 158 A GeV can one identify a small difference in the antibaryon sector ($\bar{p}$, $\bar{\Lambda} + \bar{\Sigma}^0$) in the case of 5% central Pb + Pb collisions (cf. Fig. 18).

According to the studies above, there is apparently no sizable sensitivity in the hadronic rapidity distributions to the actual differential partonic cross sections, but one has to explore the transverse dynamics in addition. To this end, we show in Figs. 20 and 21 the transverse momentum distributions for 5% central Pb + Pb collisions at 158 A GeV and midrapidity ($|y| < 0.5$) for PHSD4.0 (green lines), PHSD5.0 with partonic cross sections and parton masses calculated for $\mu_B = 0$ (blue lines), and with cross sections and parton masses evaluated at the actual chemical potential μ_B in each individual space-time cell (red lines) in comparison to the experimental data from the NA49 Collaboration [115–120]. Here, the solid lines stand for positively charged particles while the dashed lines display the results for negatively charged particles. We find that at 30 A GeV there is practically no change in the p_T spectra for all PHSD versions; only at 158 A GeV do tiny changes in the p_T spectra become visible for transverse momenta above about 2.5 GeV/c. We mention for completeness that again for 10.7 A GeV Au + Au collisions we do not find any changes also in the p_T spectra within the linewidth (cf. Fig. 19). Apparently, the space-time volume of the partonic phase is too small at AGS and SPS energies even in central Pb + Pb collisions such that one has practically no sensitivity to the microscopic collisional details in the partonic phase. However, this might
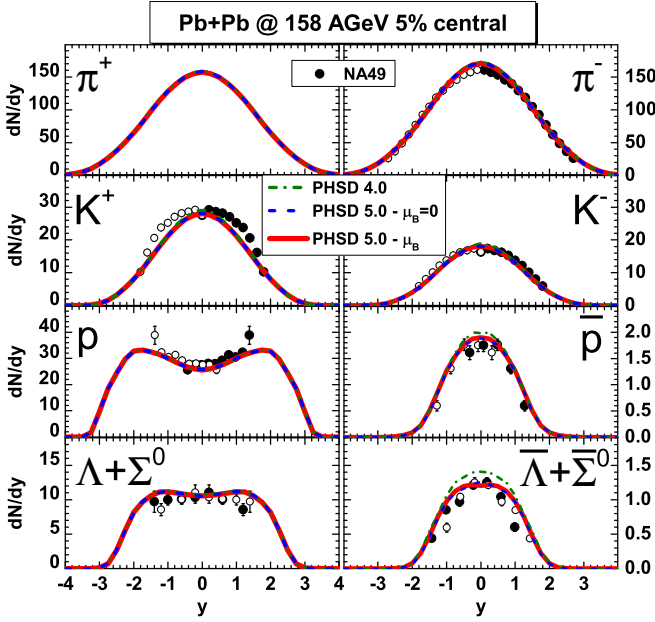
FIG. 18. The rapidity distributions for 5% central Pb + Pb collisions at 158 A GeV for PHSD4.0 (green dot-dashed lines), PHSD5.0 with partonic cross sections and parton masses calculated for $\mu_B = 0$ (blue dashed lines), and with cross sections and parton masses evaluated at the actual chemical potential μ_B in each individual space-time cell (red lines) in comparison to the experimental data from the NA49 Collaboration [118–121]. All PHSD results are the same within the linewidth except for the antibaryons.

change for ultrarelativistic collision systems where the QGP phase becomes dominant.

B. RHIC energies

As demonstrated in Ref. [60], one expects a dominantly partonic phase in central Au + Au collisions at $\sqrt{s_{NN}} = 200$ GeV especially when gating on midrapidity. However, the differences between PHSD4.0 and PHSD5.0 (with and without μ_B dependence) in the hadronic rapidity distributions for 5% central Au + Au collisions turn out to be rather small for mesons ($\pi^\pm$, $K^\pm$) and also for baryons and antibaryons (p, $\bar{p}$, $\Lambda + \Sigma^0$, $\bar{\Lambda} + \bar{\Sigma}^0$) (cf. Fig. 22) such that no robust conclusion on the partonic collisional dynamics can be drawn even in this case.

This also holds true for the transverse momentum distributions at midrapidity ($|y| < 0.5$) for these collisions when comparing the results from the different PHSD versions with each other and the data from the PHENIX [126] and STAR [127] Collaborations in Fig. 23. Only for high transverse momenta can small differences be seen with the tendency to improve the description of the data in the novel versions of PHSD5.0 with the microscopic differential partonic cross sections.

C. Asymmetric systems

Since the central collisions of the heavy systems (Au + Au or Pb + Pb) only provide information on the total partonic
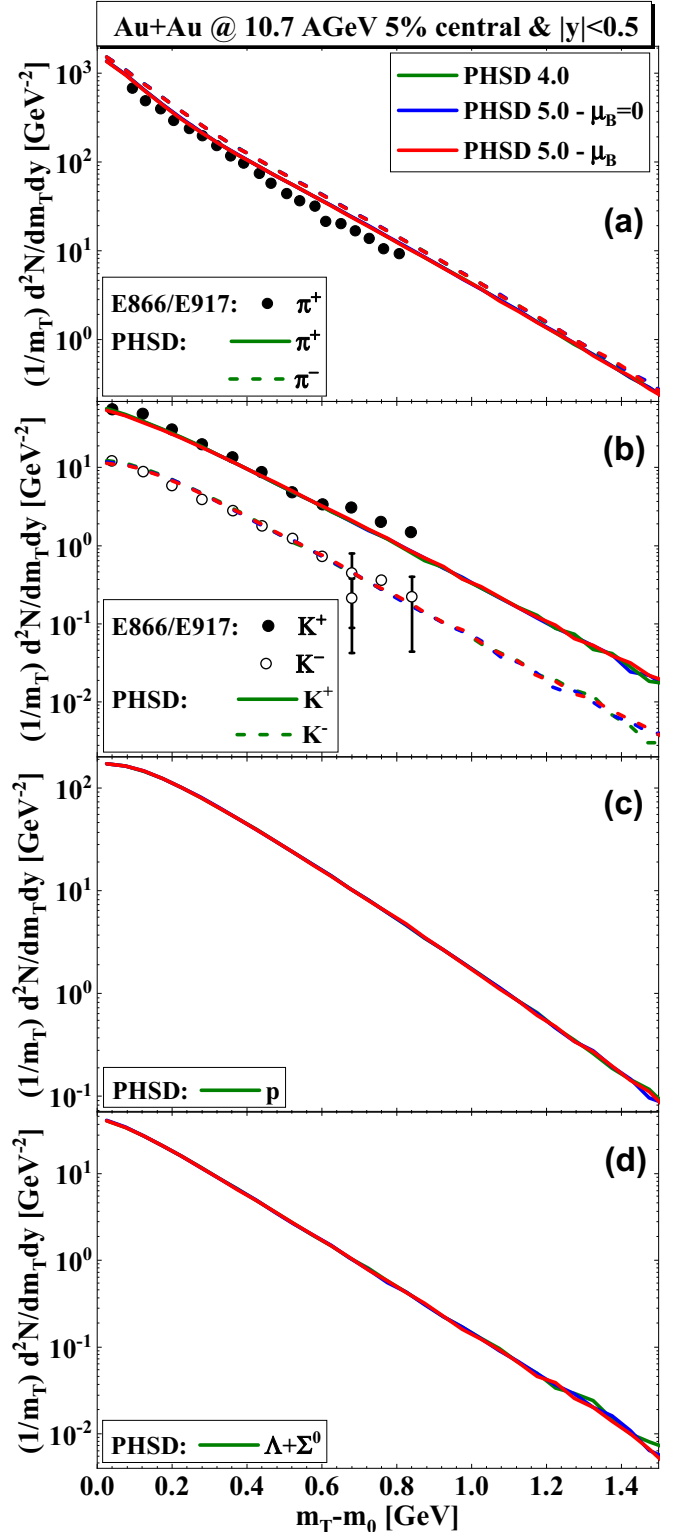
FIG. 19. The transverse momentum distributions for 5% central Pb + Pb collisions at 11 A GeV and midrapidity ($|y| < 0.5$) for PHSD4.0 (green lines), PHSD5.0 with partonic cross sections and parton masses calculated for $\mu_B = 0$ (blue lines), and with cross sections and parton masses evaluated at the actual chemical potential μ_B in each individual space-time cell (red lines) in comparison to the experimental data from the E917 and E866 Collaborations [122,123].
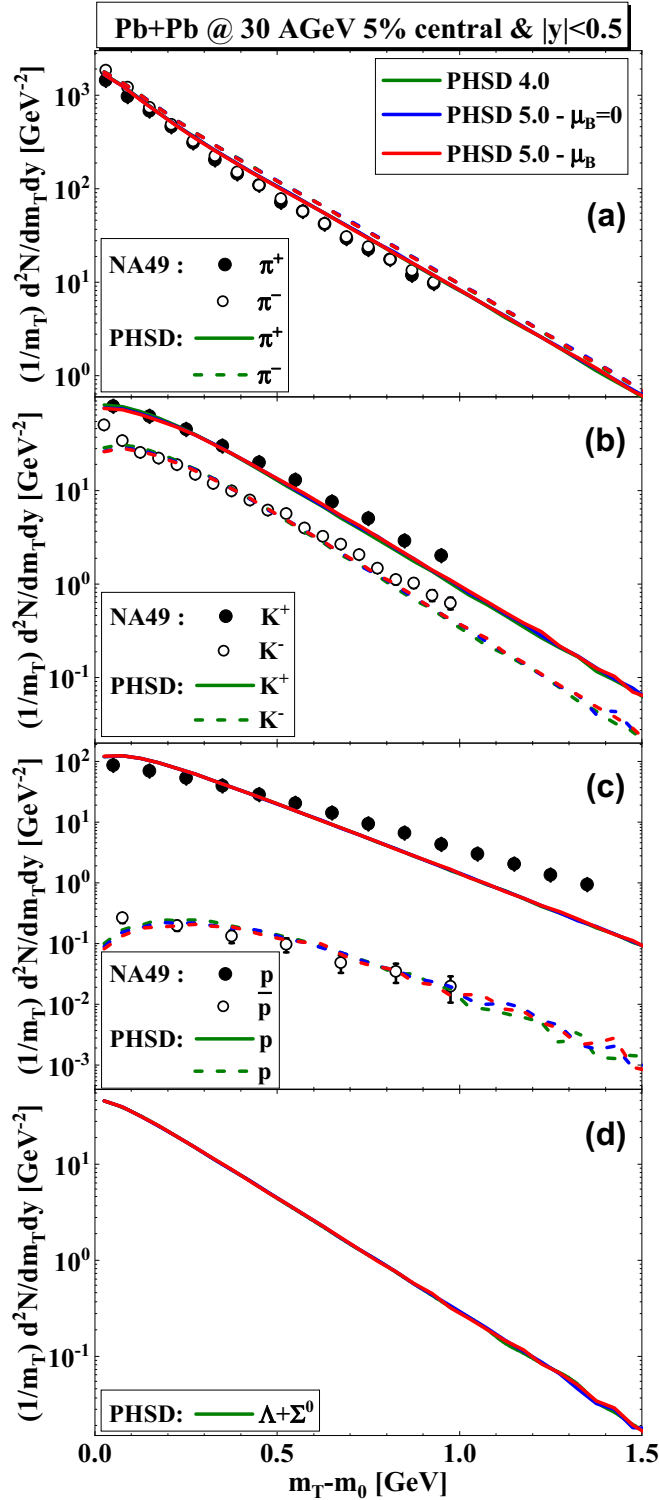
FIG. 20. The transverse momentum distributions for 5% central Pb + Pb collisions at 30 A GeV and midrapidity ($|y| < 0.5$) for PHSD4.0 (green lines), PHSD5.0 with partonic cross sections and parton masses calculated for $\mu_B = 0$ (blue lines), and with cross sections and parton masses evaluated at the actual chemical potential μ_B in each individual space-time cell (red lines) in comparison to the experimental data from the NA49 Collaboration [115–117].
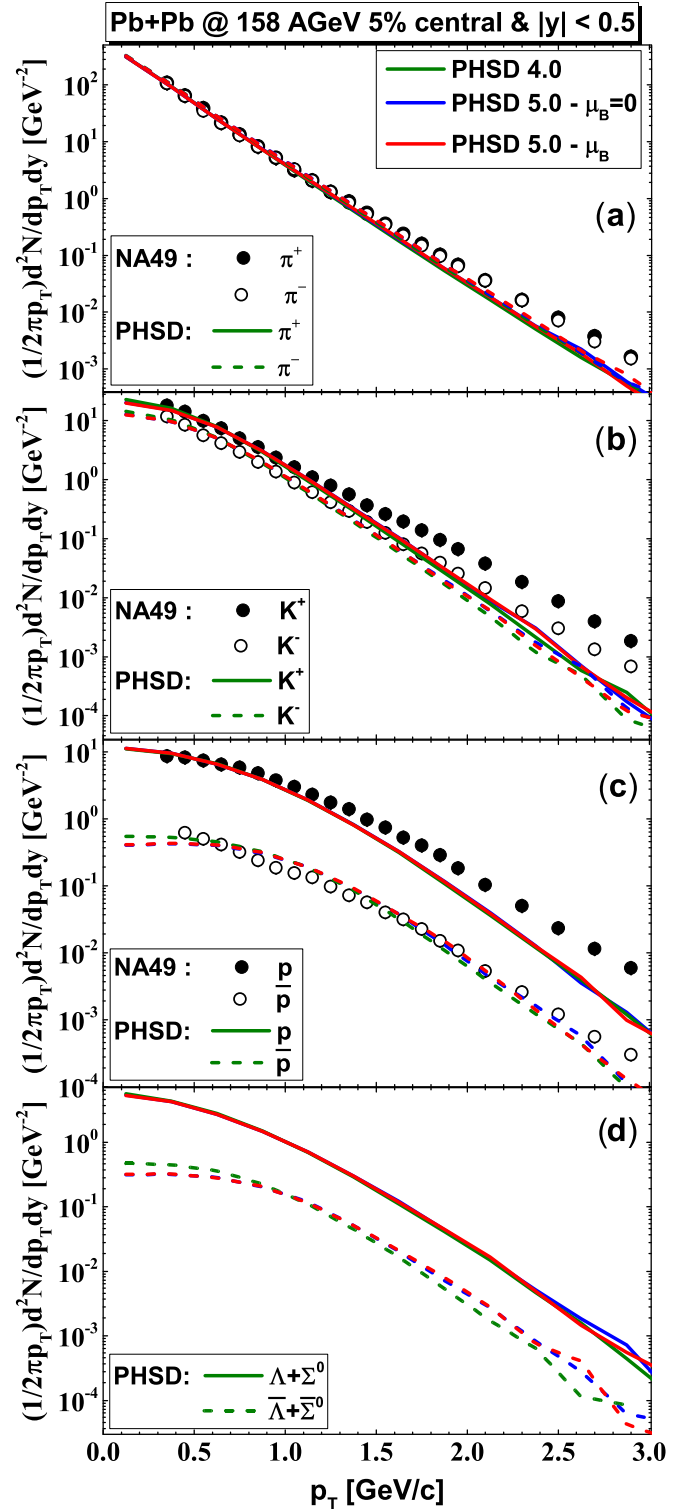
FIG. 21. The transverse momentum distributions for 5% central Pb + Pb collisions at 158 A GeV and midrapidity ($|y| < 0.5$) for PHSD4.0 (green lines), PHSD5.0 with partonic cross sections and parton masses calculated for $\mu_B = 0$ (blue lines), and with cross sections and parton masses evaluated at the actual chemical potential μ_B in each individual space-time cell (red lines) in comparison to the experimental data from the NA49 Collaboration [118–120].)
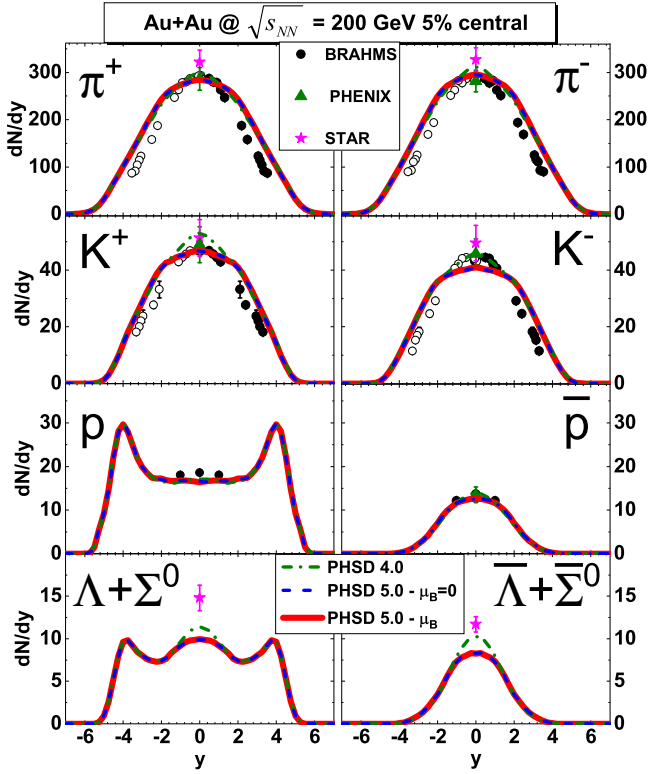
FIG. 22. The rapidity distributions for 5% central Au + Au collisions at $\sqrt{s_{NN}} = 200$ GeV for PHSD4.0 (green dot-dashed lines), PHSD5.0 with partonic cross sections and parton masses calculated for $\mu_B = 0$ (blue dashed lines), and with cross sections and parton masses evaluated at the actual chemical potential μ_B in each individual space-time cell (red lines) in comparison to the experimental data from the BRAHMS [124,125], PHENIX [126], and STAR [127] Collaborations.

reaction rate and not details of the partonic collisional dynamics, one has to explore asymmetric heavy-ion collisions—such as C + Au or Cu + Au—in addition in order find out a possible sensitivity to the partonic collisions. To this end, we have performed a systematic study of 5% C + Au and Cu + Au collisions at bombarding energies from AGS to top RHIC energies for the "bulk" observables within the different PHSD versions. We note that (without explicit representation) we did not find any difference at 10.7 and 30 A GeV as in the case of the heavy symmetric systems for the hadronic rapidity distributions and transverse momentum spectra at midrapidity. For Cu + Au, the actual results—with regard to the differences between PHSD4.0 and PHSD5.0—at all bombarding energies turned out to be very similar to the central Au + Au or Pb + Pb collisions such that an explicit representation is discarded. Only in the case of 5% C + Au reactions at top SPS and top RHIC energies have some differences been found, which will be discussed in the following.

The rapidity distributions of hadrons for 5% central C + Au collisions are displayed in Figs. 24 and 25 for 158 A GeV and $\sqrt{s_{NN}} = 200$ GeV, respectively. Note that the rapidity distributions are no longer symmetric in rapidity y but enhanced for $y < 0$ (Au-going side). There is no change of the
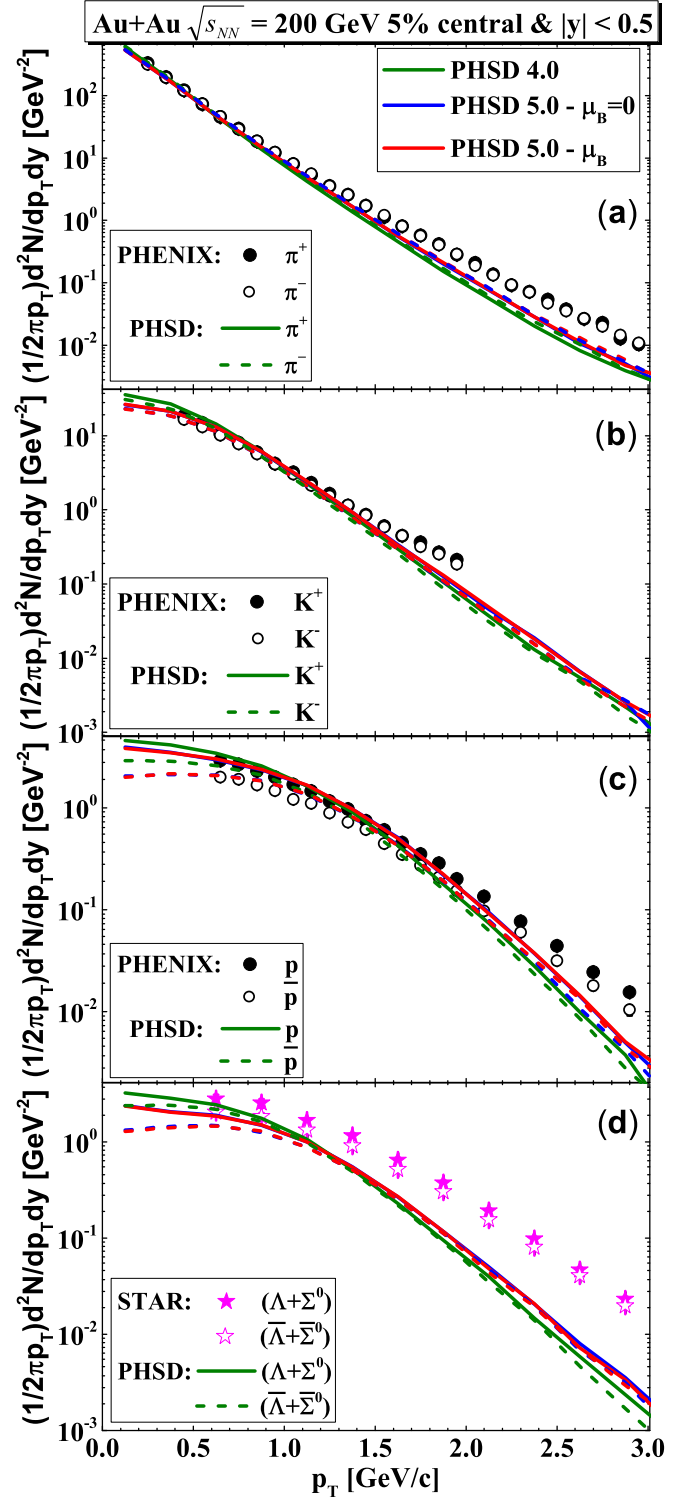
FIG. 23. The transverse momentum distributions for 5% central Au + Au collisions at $\sqrt{s_{NN}} = 200$ GeV and midrapidity ($|y| < 0.5$) for PHSD4.0 (green lines), PHSD5.0 with partonic cross sections and parton masses calculated for $\mu_B = 0$ (blue lines), and with cross sections and parton masses evaluated at the actual chemical potential μ_B in each individual space-time cell (red lines) in comparison to the experimental data from the PHENIX [126] and STAR [127] Collaborations.
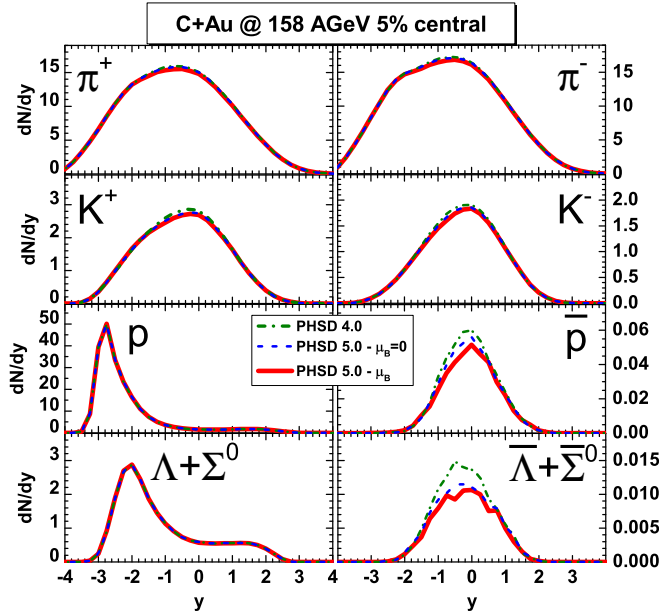
FIG. 24. The rapidity distributions for 5% central C + Au collisions at 158 A GeV for PHSD4.0 (green dot-dashed lines), PHSD5.0 with partonic cross sections and parton masses calculated for $\mu_B = 0$ (blue dashed lines), and with cross sections and parton masses evaluated at the actual chemical potential μ_B in each individual space-time cell (red lines).

FIG. 25. The rapidity distributions for 5% central C + Au collisions at $\sqrt{s_{NN}} = 200$ GeV for PHSD4.0 (green dot-dashed lines), PHSD5.0 with partonic cross sections and parton masses calculated for $\mu_B = 0$ (blue dashed lines), and with cross sections and parton masses evaluated at the actual chemical potential μ_B in each individual space-time cell (red lines).

pion and baryon distributions at both energies for the different PHSD versions as in the case of the heavy symmetric systems while tiny differences can again be seen in the antibaryon spectra. However, in the case of C + Au, now there is also a small signal in the kaon rapidity distributions which is more pronounced at $\sqrt{s_{NN}} = 200$ GeV. This suggests that the strangeness degree of freedom might be explored in very asymmetric systems to obtain additional information on the partonic scattering dynamics.

The transverse momentum spectra of hadrons at midrapidity (for C + Au) are shown in Figs. 26 and 27 for 158 A GeV and $\sqrt{s_{NN}} = 200$ GeV, respectively. There is practically no difference in the PHSD4.0 and PHSD5.0 results for pions, kaons, protons, and antiprotons and only a very small signal in the antihyperons can be identified. Nevertheless, our results for this very asymmetric system can be considered as predictions for the production of the most abundant hadron species at top SPS and RHIC energies.

VIII. SUMMARY

In this work, we have extended the PHSD transport approach (PHSD4.0 [47,57]) to incorporate differential "off-shell cross sections" for all binary partonic channels that are based on the same effective propagators and couplings as employed in the QGP equation of state and the parton propagation. To this end, we have recalled the extraction of the partonic masses and the coupling g^2 from lattice QCD data (within the DQPM) and calculated the partonic differential cross sections as a function of T and μ_B for the leading tree-level diagrams (cf. the Appendixes). Furthermore, in Sec. IV,
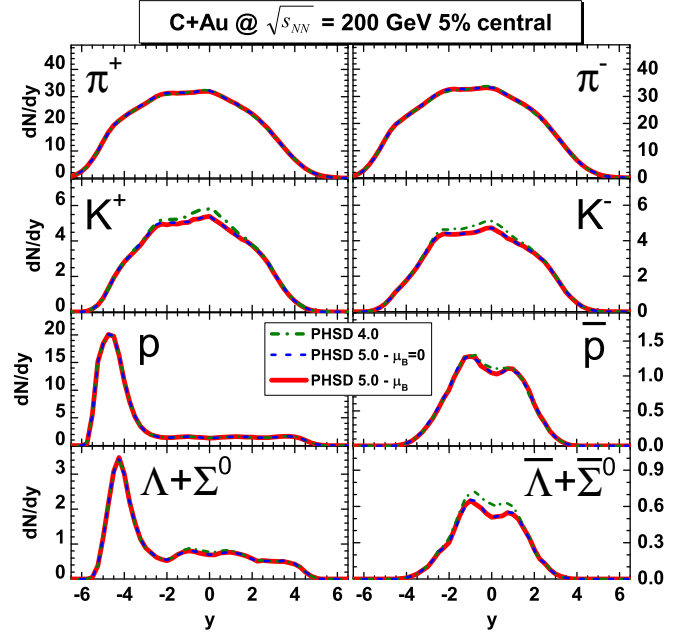
we have used these differential cross sections to evaluate partonic scattering rates for fixed T and μ_B as well as to compute the ratio of the shear viscosity η to entropy density s within the Kubo formalism in comparison to calculations from lQCD. It turns out that the ratio η/s calculated with the partonic scattering rates in the relaxation-time approximation is very similar to the original result from the DQPM and to lQCD results such that the present extension of the approach does not lead to different partonic transport properties except for temperatures close to T_c. We recall that the novel PHSD version (PHSD5.0) is practically parameter free in the partonic sector since the effective coupling (squared) is determined by a fit to the scaled entropy density from lQCD. The dynamical masses for quarks and gluons then are fixed by the HTL expressions. The interaction rate in the timelike sector is, furthermore, calculated in leading order employing the DQPM propagators and coupling.

When implementing the differential cross sections and parton masses into the PHSD5.0 approach, one has to specify the Lagrange parameters T and μ_B in each computational cell in space-time. This has been done by employing a state-of-the-art lattice QCD equation of state [102] and a diagonalization of the energy-momentum tensor from PHSD as described in Sec. V. Detailed results for T and μ_B have been presented for central collisions of Pb + Pb at $\sqrt{s_{NN}} = 17.3$ and Au + Au at $\sqrt{s_{NN}} = 200$ GeV in the (T, μ_B) plane as a function of reaction time. It turns out that the evolution of the QGP phase from the PHSD approximately follows the expectation from the isentropic trajectory $s/n_B \approx 40$ at $\sqrt{s_{NN}} = 17.3$ for
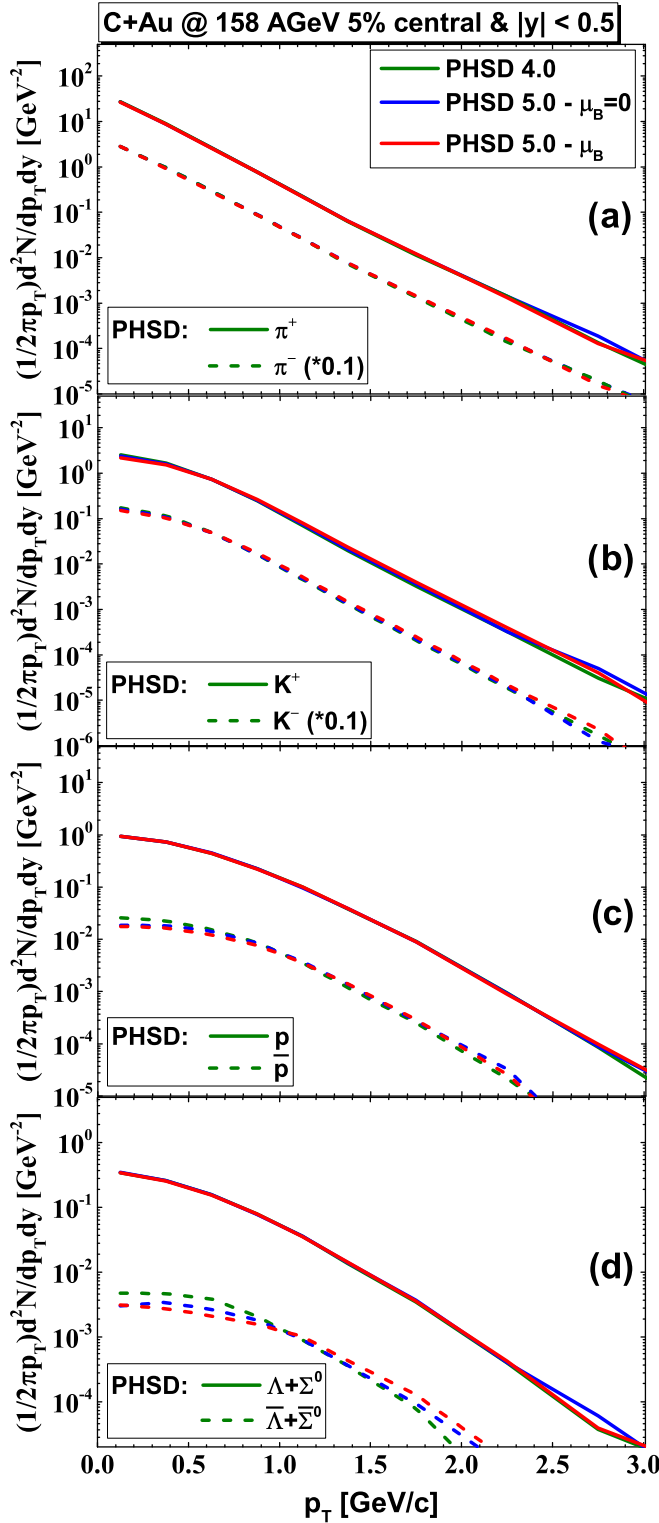
FIG. 26. The transverse momentum distributions for 5% central C + Au collisions at 158 A GeV and midrapidity ($|y| < 0.5$) for PHSD4.0 (green lines), PHSD5.0 with partonic cross sections and parton masses calculated for $\mu_B = 0$ (blue lines), and with cross sections and parton masses evaluated at the actual chemical potential μ_B in each individual space-time cell (red lines).
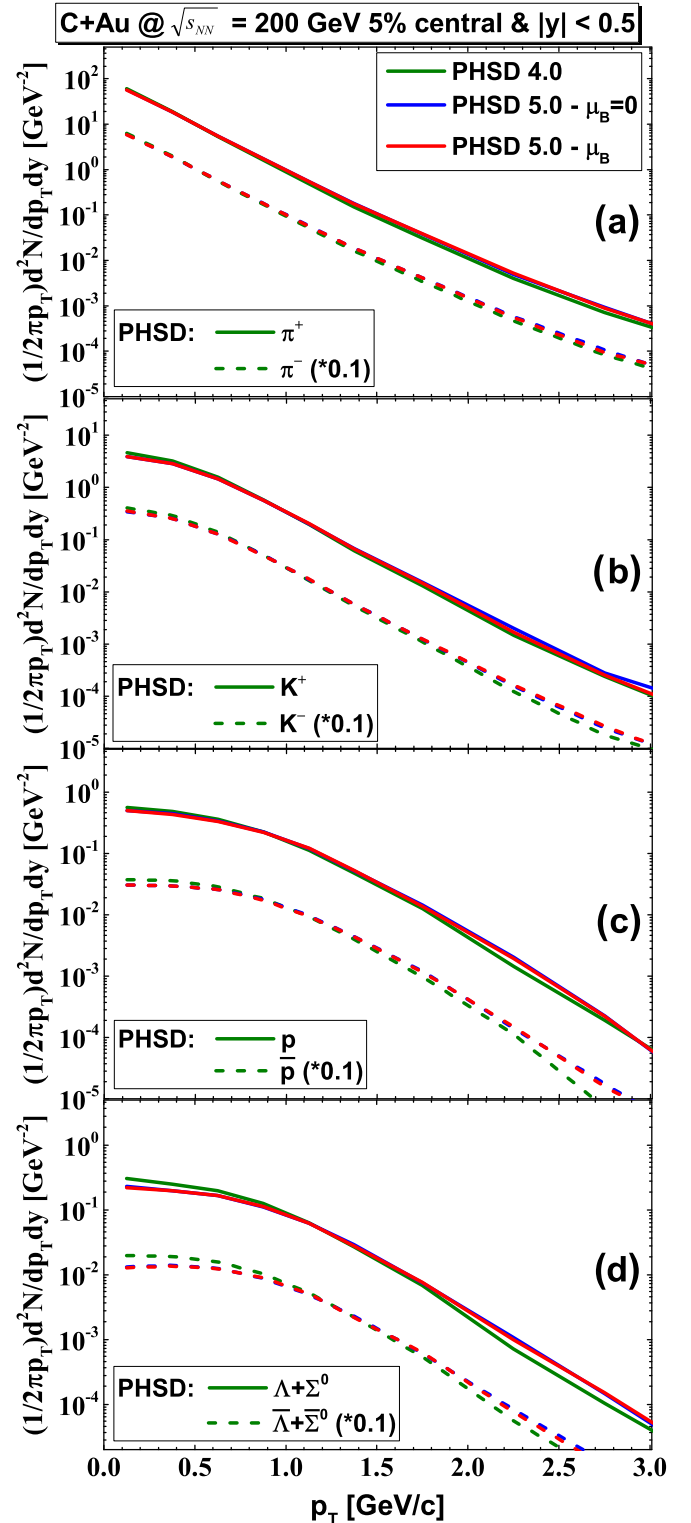
FIG. 27. The transverse momentum distributions for 5% central C + Au collisions at $\sqrt{s_{NN}} = 200$ GeV and midrapidity ($|y| < 0.5$) for PHSD4.0 (green lines), PHSD5.0 with partonic cross sections and parton masses calculated for $\mu_B = 0$ (blue lines), and with cross sections and parton masses evaluated at the actual chemical potential μ_B in each individual space-time cell (red lines).

T above T_c while at the top RHIC energy the distribution in T and μ_B spreads around zero for all reaction times considered.

In Sec. VI, we then have calculated 5% central Au + Au (or Pb + Pb) collisions and compared the results for hadronic rapidity distributions and transverse momentum spectra (at midrapidity) from the previous PHSD4.0 with the novel version PHSD5.0 (with and without the explicit dependence of the partonic differential cross sections and parton masses on μ_B). No differences for all the hadron "bulk" observables from the various PHSD versions have been found at AGS and FAIR/NICA energies within linewidth, which implies that there is no sensitivity to the new partonic differential cross sections employed. Only in the case of the kaons and the antibaryons $\bar{p}$ and $\bar{\Lambda} + \bar{\Sigma}^0$ could a small difference between PHSD4.0 and PHSD5.0 be seen at top SPS and top RHIC energies; however, there was no clear difference between the PHSD5.0 calculations with partonic cross sections for $\mu_B = 0$ and actual μ_B in the local cells. When considering very asymmetric collisions of C + Au, a small sensitivity to the partonic scatterings was found in the kaon and antibaryon rapidity distributions, too. However, it will be very hard to extract a robust signal experimentally.

Our findings can be understood as follows: The fact that we find only small traces of the μ_B dependence of partonic scattering dynamics in heavy-ion "bulk" observables—although the differential cross sections and parton masses clearly depend on μ_B—implies that one needs a sizable partonic density and large space-time QGP volume to explore the dynamics in the QGP phase. These conditions are only fulfilled at high bombarding energies (top SPS, RHIC energies) where, however, μ_B is rather low. On the other hand, decreasing the bombarding energy to FAIR-NICA energies and thus increasing μ_B lead to collisions that are dominated by the hadronic phase where the extraction of information about the parton dynamics will be rather complicated based on "bulk" observables. Further investigations of other observables (such as flow coefficients v_n of particles and antiparticles, fluctuations, and correlations) might contain more visible μ_B traces

from the QGP phase and will be the subject of a forthcoming study.

APPENDIX A: MATRIX ELEMENTS FOR $qq' \rightarrow qq'$ SCATTERING

Here, we give the details on the calculation of the matrix elements used to evaluate the DQPM partonic cross sections which are based on Refs. [68,128,129]. We recall that the Mandelstam variables are given by the momenta as $s = (k_i + p_i)^2 = (k_f + p_f)^2$, $t = (k_i - k_f)^2 = (p_i - p_f)^2$, $u = (k_i - p_f)^2 = (p_i - k_f)^2$. The generators of SU(3) associated with QCD are denoted by the matrices $T^a = \lambda^a/2$ with a being the gluon color and λ^a the Gell-Mann matrices [130]. The Lie algebra formed by the generators T^a is given by the commutation relation $[T^a, T^b] = if^{abc}T^c$ where f^{abc} are the structure constants. We refer the reader to Ref. [131] where all the rules for calculating the color factors in the following calculations are given in detail. The γ matrices are denoted by γ^μ and the Dirac spinors are u for particles and v for antiparticles. The final analytical expressions for the matrix elements used in the PHSD code were evaluated using FEYNCALC [132,133].

The invariant matrix elements corresponding to Fig. 28 are given by the following expressions:

$$i\mathcal{M}_t\big(q_\alpha^i q_\beta^k \rightarrow q_\delta^j q_\gamma^l\big) = \delta_{\alpha\delta}\,\delta_{\beta\gamma}\,\bar{u}_\delta^j(k_f)\big(-ig\gamma^\mu T_{ij}^a\big)u_\alpha^i(k_i)\left[-i\frac{g_{\mu\nu} - (q_\mu^t q_\nu^t)/M_g^2}{(k_f - k_i)^2 - M_g^2 + 2i\gamma_g\omega_t}\right]\bar{u}_\gamma^l(p_f)\big(-ig\gamma^\nu T_{kl}^a\big)u_\beta^k(p_i), \quad \text{(A1)}$$

$$i\mathcal{M}_u\big(q_\alpha^i q_\beta^k \rightarrow q_\delta^j q_\gamma^l\big) = -\delta_{\alpha\beta}\,\delta_{\alpha\delta}\,\delta_{\beta\gamma}\,\bar{u}_\delta^j(k_f)\big(-ig\gamma^\nu T_{kj}^a\big)u_\beta^k(p_i)\left[-i\frac{g_{\mu\nu} - (q_\mu^u q_\nu^u)/M_g^2}{(p_f - k_i)^2 - M_g^2 + 2i\gamma_g\omega_u}\right]\bar{u}_\gamma^l(p_f)\big(-ig\gamma^\mu T_{il}^a\big)u_\alpha^i(k_i),$$

$$\text{(A2)}$$

$$i\mathcal{M}_s\big(q_\alpha^i q_\beta^k \rightarrow q_\delta^j q_\gamma^l\big) = -\delta_{\alpha\bar{\beta}}\,\delta_{\delta\bar{\gamma}}\,\bar{u}_\delta^j(k_f)\big(-ig\gamma^\nu T_{lj}^a\big)v_\gamma^l(p_f)\left[-i\frac{g_{\mu\nu} - (q_\mu^s q_\nu^s)/M_g^2}{(k_i + p_i)^2 - M_g^2 + 2i\gamma_g\omega_s}\right]\bar{v}_\beta^k(p_i)\big(-ig\gamma^\mu T_{ik}^a\big)u_\alpha^i(k_i), \quad \text{(A3)}$$

where the energy of the exchanged gluon is $\omega_t = |k_f^0 - k_i^0|$, $\omega_u = |p_f^0 - k_i^0|$, and $\omega_s = |k_i^0 + p_i^0|$, and its momentum denoted by $q_t^\mu = (k_f - k_i)^\mu$, $q_u^\mu = (p_i - k_f)^\mu$, and $q_s^\mu = (k_i + p_i)^\mu$. We note here that the matrix element $\mathcal{M}_t$ given above only corresponds to a q-q elastic scattering, but the final contribution from t-channel diagrams to $|\overline{\mathcal{M}}|^2$ is found to be the same whether a quark
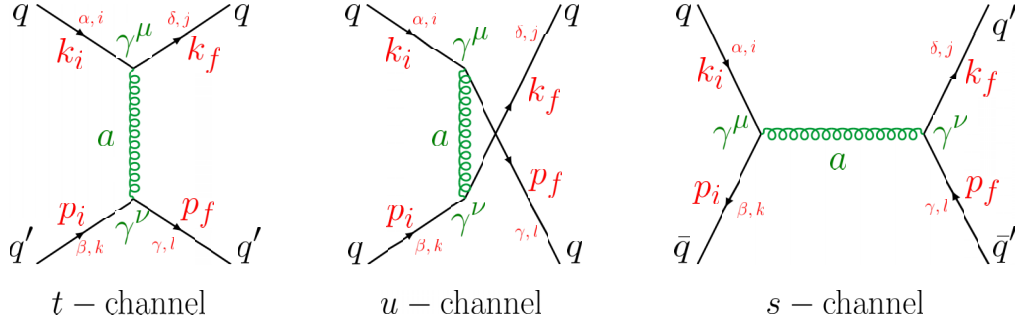
FIG. 28. Leading-order Feynman diagrams for the $qq' \to qq'$ and $q\bar{q} \to q'\bar{q}'$ processes. The initial and final 4-momenta are k_i and p_i, and k_f and p_f, respectively. The indices $i, j, k, l = 1$–3 denote the quark colors, $a = 1$–8 denote the gluon colors, while the quark flavor is indicated by the indices $\alpha, \beta, \delta, \gamma = u, d, s, ...$

scatters with a quark or antiquark since the amplitudes are averaged (summed) over initial (final) partons as

$$|\bar{\mathcal{M}}(q_\alpha q_\beta \to q_\delta q_\gamma)|^2 = \frac{1}{d_q^2} \sum_{\text{color}} \sum_{\text{spin}} |\mathcal{M}_t + \mathcal{M}_u + \mathcal{M}_s|^2$$

$$= \frac{1}{3 \times 3} \sum_{\text{color}} \frac{1}{2 \times 2} \sum_{\text{spin}} (|\mathcal{M}_t|^2 + |\mathcal{M}_u|^2 + 2\,\text{Re}\,[\mathcal{M}_t \mathcal{M}_u^\star] + 2\,\text{Re}\,[\mathcal{M}_t \mathcal{M}_s^\star]). \tag{A4}$$

APPENDIX B: MATRIX ELEMENTS FOR $gq \to gq$ SCATTERING

The invariant matrix elements corresponding to the Feynman diagrams in Fig. 29 are given by the following expressions:

$$i\mathcal{M}_t(g^a q^i \to g^b q^j) = (\epsilon_{b,f}^\star)_\nu [-gf^{cab}C^{\lambda\mu\nu}(k_i - k_f, -k_i, k_f)](\epsilon_{a,i})_\mu \left[-i\frac{g_{\lambda\tau} - (q_\lambda^t q_\tau^t)/M_g^2}{(k_f - k_i)^2 - M_g^2 + 2i\gamma_g\omega_t} \right] \bar{u}^j(p_f)(-ig\gamma^\tau T_{ij}^c)u^i(p_i),$$
$$\tag{B1}$$

$$i\mathcal{M}_u(g^a q^i \to g^b q^j) = \bar{u}^j(p_f)(-ig\gamma^\mu T_{kj}^a)(\epsilon_{a,i})_\mu \left[i\frac{\slashed{q}^u + M_q}{u - M_q^2 + 2i\gamma_q\omega_u} \right] (\epsilon_{b,f}^\star)_\nu (-ig\gamma^\nu T_{ik}^b)u^i(p_i), \tag{B2}$$

$$i\mathcal{M}_s(g^a q^i \to g^b q^j) = \bar{u}^j(p_f)(-ig\gamma^\nu T_{lj}^b)(\epsilon_{b,f}^\star)_\nu \left[i\frac{\slashed{q}^s + M_q}{s - M_q^2 + 2i\gamma_q\omega_s} \right] (\epsilon_{a,i})_\mu (-ig\gamma^\mu T_{il}^a)u^i(p_i), \tag{B3}$$

with the 3-gluon vertex $C^{\lambda\mu\nu}(q_1, q_2, q_3) = [(q_1 - q_2)^\nu g^{\lambda\mu} + (q_2 - q_3)^\lambda g^{\mu\nu} + (q_3 - q_1)^\mu g^{\lambda\nu}]$ and the momentum of the exchanged gluon $q_t^\mu = (k_f - k_i)^\mu$ in the t-channel.
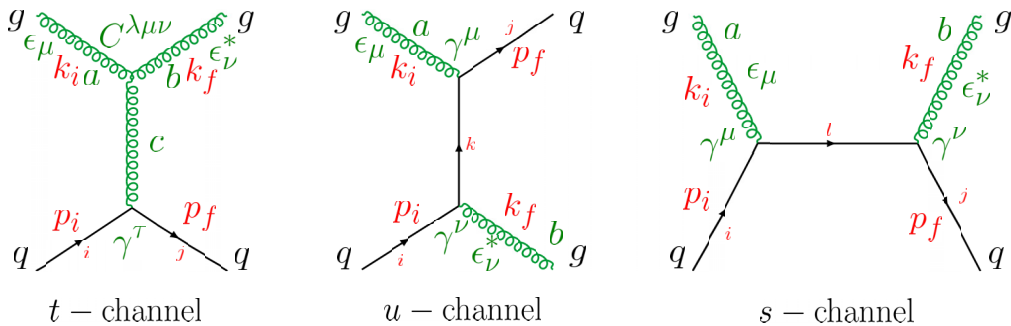
FIG. 29. Leading-order Feynman diagrams for the $gq \to gq$ processes. The initial and final 4-momenta are k_i and p_i, and k_f and p_f, respectively. The indices $i, j, k, l = 1$–3 denote the quark colors, $a, b, c = 1$–8 indicate the gluon colors, while the quark flavor is indicated by the indices $\alpha, \beta, \delta, \gamma = u, d, s, ...$
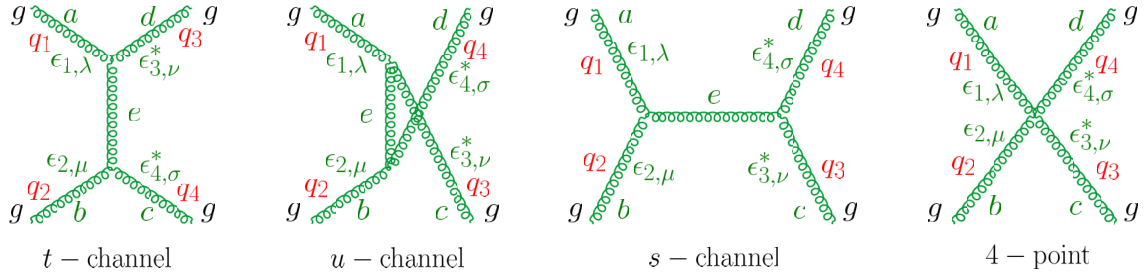
FIG. 30. Leading-order Feynman diagrams for the $gg \to gg$ scatterings. The initial and final 4-momenta are k_i and p_i, and k_f and p_f, respectively. The indices $a, b, c, d, e = 1$–8 denote the gluon colors.

In the case of a massive gluon, the sum over polarizations is given by [in accordance with the denominator of the propagator in Eq. (27)]

$$\sum_{\text{pol.}} (\epsilon_i)_\mu (\epsilon_i^\star)_{\mu'} = -g_{\mu\mu'} + \frac{(k_i)_\mu (k_i)_{\mu'}}{(M_i)_g^2}. \tag{B4}$$

The invariant matrix element squared averaged (summed) over the initial (final) partons is

$$|\overline{\mathcal{M}}(gq \to gq)|^2 = \frac{1}{d_g d_q} \sum_{\text{color}} \sum_{\text{spin}} |\mathcal{M}_t + \mathcal{M}_u + \mathcal{M}_s|^2$$

$$= \frac{1}{8 \times 3} \sum_{\text{color}} \frac{1}{2 \times 2} \sum_{\text{spin}} (|\mathcal{M}_t|^2 + |\mathcal{M}_u|^2 + |\mathcal{M}_s|^2 + 2\,\text{Re}\,[\mathcal{M}_t \mathcal{M}_u^\star] + 2\,\text{Re}\,[\mathcal{M}_t \mathcal{M}_s^\star] + 2\,\text{Re}\,[\mathcal{M}_u \mathcal{M}_s^\star]). \tag{B5}$$

APPENDIX C: MATRIX ELEMENTS FOR $gg \to gg$ SCATTERING

The invariant matrix elements corresponding to the Feynman diagrams in Fig. 30 are given by the following expressions:

$$i\mathcal{M}_t(g^a g^b \to g^c g^d) = (\epsilon_{d,4}^\star)_\sigma [-gf^{ead} C^{\tau\lambda\sigma}(q_1 - q_4, -q_1, q_4)](\epsilon_{a,1})_\lambda$$
$$\times \left[-i \frac{g_{\tau\tau'} - (q_\tau^t q_{\tau'}^t)/M_g^2}{(q_4 - q_1)^2 - M_g^2 + 2i\gamma_g \omega_t} \right] (\epsilon_{c,3}^\star)_\nu [-gf^{ecb} C^{\tau'\nu\mu}(-q_3 + q_2, q_3, -q_2)](\epsilon_{b,2})_\mu, \tag{C1}$$

$$i\mathcal{M}_s(g^a g^b \to g^c g^d) = (\epsilon_{d,4}^\star)_\sigma [-gf^{edc} C^{\tau'\sigma\nu}(-q_4 - q_3, q_4, q_3)](\epsilon_{c,3}^\star)_\nu$$
$$\times \left[-i \frac{g_{\tau\tau'} - (q_\tau^s q_{\tau'}^s)/M_g^2}{(q_1 + q_2)^2 - M_g^2 + 2i\gamma_g \omega_s} \right] (\epsilon_{b,2})_\mu [-gf^{eba} C^{\tau\mu\lambda}(q_2 + q_1, -q_2, -q_1)](\epsilon_{a,1})_\lambda \tag{C2}$$

$$i\mathcal{M}_u(g^a g^b \to g^c g^d) = (\epsilon_{d,4}^\star)_\sigma [-gf^{edb} C^{\tau'\sigma\mu}(-q_4 + q_2, q_4, -q_2)](\epsilon_{b,2})_\mu$$
$$\times \left[-i \frac{g_{\tau\tau'} - (q_\tau^u q_{\tau'}^u)/M_g^2}{(q_2 - q_4)^2 - M_g^2 + 2i\gamma_g \omega_u} \right] (\epsilon_{c,3}^\star)_\nu [-gf^{eac} C^{\tau\lambda\nu}(q_1 - q_3, -q_1, q_3)](\epsilon_{a,1})_\lambda, \tag{C3}$$

with the 3-gluon vertex $C^{\lambda\mu\nu}(q_1, q_2, q_3) = [(q_1 - q_2)^\nu g^{\lambda\mu} + (q_2 - q_3)^\lambda g^{\mu\nu} + (q_3 - q_1)^\mu g^{\lambda\nu}]$ and the momentum of the exchanged gluon $q_t^\mu = (q_4 - q_1)^\mu$, $q_s^\mu = (q_1 + q_2)^\mu$, and $q_u^\mu = (q_2 - q_4)^\mu$.

The 4-point invariant amplitude is given by (according to Refs. [128,129])

$$i\mathcal{M}_4(g^a g^b \to g^c g^d) = -ig^2 [f^{abe} f^{cde}(g^{\lambda\nu} g^{\mu\sigma} - g^{\lambda\sigma} g^{\mu\nu}) + f^{ace} f^{bde}(g^{\lambda\mu} g^{\nu\sigma} - g^{\lambda\sigma} g^{\nu\mu})$$
$$+ f^{ade} f^{cbe}(g^{\lambda\mu} g^{\sigma\nu} - g^{\lambda\nu} g^{\sigma\mu})](\epsilon_{d,4}^\star)_\sigma (\epsilon_{c,3}^\star)_\nu (\epsilon_{b,2})_\mu (\epsilon_{a,1})_\lambda,$$

$$\mathcal{M}_4(g^a g^b \to g^c g^d) = f^{abe} f^{cde} \mathcal{M}_4^s + f^{ace} f^{bde} \mathcal{M}_4^u + f^{ade} f^{cbe} \mathcal{M}_4^t. \tag{C4}$$

The invariant matrix element squared averaged (summed) over the initial (final) gluons is

$$|\overline{\mathcal{M}}(gg \to gg)|^2 = \frac{1}{d_g^2} \sum_{\text{color}} \sum_{\text{spin}} |\mathcal{M}(g^a g^b \to g^c g^d)|^2$$

$$= \frac{1}{8 \times 8} \sum_{\text{color}} \frac{1}{2 \times 2} \sum_{\text{spin}} (|\mathcal{M}_t|^2 + |\mathcal{M}_s|^2 + |\mathcal{M}_u|^2 + |\mathcal{M}_4|^2 + 2\,\text{Re}\,[\mathcal{M}_t \mathcal{M}_s^\star] + 2\,\text{Re}\,[\mathcal{M}_t \mathcal{M}_u^\star]$$

$$+ 2\,\text{Re}\,[\mathcal{M}_u \mathcal{M}_s^\star] + 2\,\text{Re}\,[\mathcal{M}_t \mathcal{M}_4^\star] + 2\,\text{Re}\,[\mathcal{M}_s \mathcal{M}_4^\star] + +2\,\text{Re}\,[\mathcal{M}_u \mathcal{M}_4^\star]). \tag{C5}$$

[1] J. S. Schwinger, J. Math. Phys. **2**, 407 (1961).
[2] P. M. Bakshi and K. T. Mahanthappa, J. Math. Phys. **4**, 12 (1963).
[3] L. V. Keldysh, Zh. Eksp. Teor. Fiz. **47**, 1515 (1964) [Sov. Phys. JETP **20**, 1018 (1965)].
[4] R. A. Craig, J. Math. Phys. **9**, 605 (1968).
[5] M. Bonitz, *Quantum Kinetic Theory*, Teubner Texte zur Physik (Vieweg+Teubner Verlag, Stuttgart, Leipzig, 1998).
[6] L. P. Kadanoff and G. Baym, *Quantum Statistical Mechanics* (W. A. Benjamin, New York, 1962).
[7] D. DuBois, in *Lectures in Theoretical Physics*, edited by W. E. Brittin (Gordon and Breach, London, 1967).
[8] P. Danielewicz, Ann. Phys. **152**, 305 (1984).
[9] K.-c. Chou, Z.-b. Su, B.-l. Hao, and L. Yu, Phys. Rep. **118**, 1 (1985).
[10] J. Rammer and H. Smith, Rev. Mod. Phys. **58**, 323 (1986).
[11] E. Calzetta and B. L. Hu, Phys. Rev. D **37**, 2878 (1988).
[12] H. Haug and A. Jauho, *Quantum Kinetics in Transport and Optics of Semiconductors*, Springer Series in Solid-State Sciences (Springer, Berlin, 1998).
[13] B. Bezzerides and D. DuBois, Ann. Phys. **70**, 10 (1972).
[14] W. Botermans and R. Malfliet, Phys. Rep. **198**, 115 (1990).
[15] S. Mrowczynski and P. Danielewicz, Nucl. Phys. B **342**, 345 (1990).
[16] A. Makhlin and E. Surdutovich, Phys. Rev. C **58**, 389 (1998).
[17] A. Makhlin, Phys. Rev. C **52**, 995 (1995).
[18] K. Geiger, Phys. Rev. D **54**, 949 (1996).
[19] K. Geiger, Phys. Rev. D **56**, 2665 (1997).
[20] D. A. Brown and P. Danielewicz, Phys. Rev. D **58**, 094003 (1998).
[21] J.-P. Blaizot and E. Iancu, Nucl. Phys. B **557**, 183 (1999).
[22] W. Cassing and S. Juchem, Nucl. Phys. A **665**, 377 (2000).
[23] W. Cassing and S. Juchem, Nucl. Phys. A **672**, 417 (2000).
[24] Yu. B. Ivanov, J. Knoll, and D. N. Voskresensky, Nucl. Phys. A **657**, 413 (1999).
[25] J. Knoll, Yu. B. Ivanov, and D. N. Voskresensky, Ann. Phys. **293**, 126 (2001).
[26] W. Cassing, Eur. Phys. J. ST **168**, 3 (2009).
[27] H. A. Weldon, Phys. Rev. D **28**, 2007 (1983).
[28] V. V. Lebedev and A. V. Smilga, Ann. Phys. **202**, 229 (1990).
[29] E. Braaten and R. D. Pisarski, Phys. Rev. D **42**, 2156 (1990).
[30] E. Braaten and R. D. Pisarski, Phys. Rev. D **46**, 1829 (1992).
[31] R. D. Pisarski, Phys. Rev. D **47**, 5589 (1993).
[32] S. Jeon, Phys. Rev. D **52**, 3591 (1995).
[33] E.-k. Wang and U. W. Heinz, Phys. Rev. D **53**, 899 (1996).
[34] M. H. Thoma, Phys. Rev. D **49**, 451 (1994).
[35] S. Y. F. Liu and R. Rapp, Phys. Rev. C **97**, 034918 (2018).
[36] B. Vanderheyden and G. Baym, J. Stat. Phys. **93**, 843 (1998).
[37] C. Bernard, T. Burch, E. B. Gregory, D. Toussaint, C. E. DeTar, J. Osborn, S. Gottlieb, U. M. Heller, and R. Sugar, Phys. Rev. D **71**, 034504 (2005).
[38] Y. Aoki, G. Endrodi, Z. Fodor, S. D. Katz, and K. K. Szabo, Nature (London) **443**, 675 (2006).
[39] A. Bazavov, T. Bhattacharya, M. Cheng, C. DeTar, H.-T. Ding, S. Gottlieb, R. Gupta, P. Hegde, U. M. Heller, F. Karsch, E. Laermann, L. Levkova, S. Mukherjee, P. Petreczky, C. Schmidt, R. A. Soltz, W. Soeldner, R. Sugar, D. Toussaint, W. Unger *et al.* (HotQCD Collaboration), Phys. Rev. D **85**, 054503 (2012).
[40] C. S. Fischer and J. Luecker, Phys. Lett. B **718**, 1036 (2013).
[41] C. S. Fischer, Prog. Part. Nucl. Phys. **105**, 1 (2019).
[42] P. Senger, E. Bratkovskaya, A. Andronic, R. Averbeck, R. Bellwied, V. Friese, C. Fuchs, J. Knoll, J. Randrup, and J. Steinheimer, Lect. Notes Phys. **814**, 681 (2011).
[43] M. Ruggieri, L. Oliva, P. Castorina, R. Gatto, and V. Greco, Phys. Lett. B **734**, 255 (2014).
[44] B. Mohanty (STAR Collaboration), J. Phys. G **38**, 124023 (2011).
[45] L. Kumar (STAR Collaboration), J. Phys. G **38**, 124145 (2011).
[46] W. Cassing, A. Palmese, P. Moreau, and E. L. Bratkovskaya, Phys. Rev. C **93**, 014902 (2016).
[47] A. Palmese, W. Cassing, E. Seifert, T. Steinert, P. Moreau, and E. L. Bratkovskaya, Phys. Rev. C **94**, 044912 (2016).
[48] C. Shen and B. Schenke, Nucl. Phys. A **982**, 411 (2019).
[49] M. Li and C. Shen, Phys. Rev. C **98**, 064908 (2018).
[50] Yu. B. Ivanov, V. N. Russkikh, and V. D. Toneev, Phys. Rev. C **73**, 044904 (2006).
[51] Yu. B. Ivanov and D. Blaschke, Phys. Rev. C **92**, 024916 (2015).
[52] G. S. Denicol, C. Gale, S. Jeon, A. Monnai, B. Schenke, and C. Shen, Phys. Rev. C **98**, 034916 (2018).
[53] H. Petersen, J. Steinheimer, G. Burau, M. Bleicher, and H. Stöcker, Phys. Rev. C **78**, 044901 (2008).
[54] I. Karpenko, Acta Phys. Pol. B **50**, 141 (2019).
[55] M. Li and J. I. Kapusta, Phys. Rev. C **99**, 014906 (2019).
[56] W. Cassing and E. L. Bratkovskaya, Nucl. Phys. A **831**, 215 (2009).
[57] O. Linnyk, E. L. Bratkovskaya, and W. Cassing, Prog. Part. Nucl. Phys. **87**, 50 (2016).
[58] V. Ozvenchuk, O. Linnyk, M. I. Gorenstein, E. L. Bratkovskaya, and W. Cassing, Phys. Rev. C **87**, 024901 (2013).
[59] O. Linnyk, W. Cassing, J. Manninen, E. L. Bratkovskaya, P. B. Gossiaux, J. Aichelin, T. Song, and C. M. Ko, Phys. Rev. C **87**, 014905 (2013).
[60] E. L. Bratkovskaya, W. Cassing, V. P. Konchakovski, and O. Linnyk, Nucl. Phys. A **856**, 162 (2011).
[61] V. P. Konchakovski, W. Cassing, and V. D. Toneev, J. Phys. G **42**, 055106 (2015).
[62] V. P. Konchakovski, E. L. Bratkovskaya, W. Cassing, V. Toneev, and V. Voronyuk, Phys. Rev. C **85**, 011902(R) (2012).
[63] V. P. Konchakovski, E. L. Bratkovskaya, W. Cassing, V. D. Toneev, S. A. Voloshin, and V. Voronyuk, Phys. Rev. C **85**, 044922 (2012).
[64] V. P. Konchakovski, W. Cassing, Yu. B. Ivanov, and V. D. Toneev, Phys. Rev. C **90**, 014903 (2014).
[65] H. Berrehrah, W. Cassing, E. Bratkovskaya, and T. Steinert, Phys. Rev. C **93**, 044914 (2016).
[66] H. Berrehrah, E. Bratkovskaya, T. Steinert, and W. Cassing, Int. J. Mod. Phys. E **25**, 1642003 (2016).
[67] S. S. Adler *et al.* (PHENIX Collaboration), Phys. Rev. Lett. **91**, 182301 (2003).
[68] H. Berrehrah, E. Bratkovskaya, W. Cassing, P. B. Gossiaux, J. Aichelin, and M. Bleicher, Phys. Rev. C **89**, 054901 (2014).
[69] H. Berrehrah, E. Bratkovskaya, W. Cassing, and R. Marty, J. Phys.: Conf. Ser. **612**, 012050 (2015).
[70] H. Berrehrah, E. Bratkovskaya, W. Cassing, P. B. Gossiaux, and J. Aichelin, Phys. Rev. C **91**, 054902 (2015).
[71] O. Kaczmarek, F. Karsch, F. Zantow, and P. Petreczky, Phys. Rev. D **70**, 074505 (2004); **72**, 059903 (2005).

[72] S. Borsanyi, G. Endrodi, Z. Fodor, S. D. Katz, S. Krieg, C. Ratti, and K. K. Szabo, J. High Energy Phys. 08 (2012) 053.

[73] S. Borsanyi, Z. Fodor, C. Hoelbling, S. D. Katz, S. Krieg, and K. K. Szabo, Phys. Lett. B **730**, 99 (2014).

[74] F. Karsch, PoS **CPOD2013**, 046 (2013).

[75] A. Bazavov, H.-T. Ding, P. Hegde, O. Kaczmarek, F. Karsch, E. Laermann, Y. Maezawa, S. Mukherjee, H. Ohno, P. Petreczky, H. Sandmeyer, P. Steinbrecher, C. Schmidt, S. Sharma, W. Soeldner, and M. Wagner, Phys. Rev. D **95**, 054504 (2017).

[76] T. Steinert and W. Cassing, J. Phys.: Conf. Ser. **1024**, 012029 (2018).

[77] L. Adamczyk *et al.* (STAR Collaboraion), Phys. Rev. C **96**, 044904 (2017).

[78] W. Cassing, Nucl. Phys. A **795**, 70 (2007).

[79] M. L. Bellac, *Thermal Field Theory*, Cambridge Monographs on Mathematical Physics (Cambridge University Press, Cambridge, UK, 2011).

[80] R. D. Pisarski, Physica A (Amsterdam, Neth.) **158**, 146 (1989).

[81] J. P. Blaizot, E. Iancu, and A. Rebhan, Phys. Rev. D **63**, 065003 (2001).

[82] L. Rauber and W. Cassing, Phys. Rev. D **89**, 065008 (2014).

[83] E. Braaten and M. H. Thoma, Phys. Rev. D **44**, 1298 (1991).

[84] P. Chakraborty and J. I. Kapusta, Phys. Rev. C **83**, 014906 (2011).

[85] R. Kubo, J. Phys. Soc. Jpn. **12**, 570 (1957).

[86] D. Zubarev, V. Morozov, and G. Röpke, *Statistical Mechanics of Nonequilibrium Processes: Relaxation and Hydrodynamic Processes* (Akademie Verlag, Berlin, 1996).

[87] G. Aarts and J. M. Martinez Resco, J. High Energy Phys. 04 (2002) 053.

[88] M. Iwasaki, H. Ohnishi, and T. Fukutome, J. Phys. G **35**, 035003 (2008).

[89] R. Lang, N. Kaiser, and W. Weise, Eur. Phys. J. A **48**, 109 (2012).

[90] R. Lang and W. Weise, Eur. Phys. J. A **50**, 63 (2014).

[91] M. Haas, L. Fister, and J. M. Pawlowski, Phys. Rev. D **90**, 091501(R) (2014).

[92] N. Christiansen, M. Haas, J. M. Pawlowski, and N. Strodthoff, Phys. Rev. Lett. **115**, 112002 (2015).

[93] V. Ozvenchuk, O. Linnyk, M. I. Gorenstein, E. L. Bratkovskaya, and W. Cassing, Phys. Rev. C **87**, 064903 (2013).

[94] C. Sasaki and K. Redlich, Phys. Rev. C **79**, 055207 (2009).

[95] C. Sasaki and K. Redlich, Nucl. Phys. A **832**, 62 (2010).

[96] M. Bluhm, B. Kämpfer, and K. Redlich, Nucl. Phys. A **830**, 737c (2009).

[97] M. Bluhm, B. Kämpfer, and K. Redlich, Phys. Rev. C **84**, 025201 (2011).

[98] M. Albright and J. I. Kapusta, Phys. Rev. C **93**, 014903 (2016).

[99] G. Policastro, D. T. Son, and A. O. Starinets, Phys. Rev. Lett. **87**, 081601 (2001).

[100] P. K. Kovtun, D. T. Son, and A. O. Starinets, Phys. Rev. Lett. **94**, 111601 (2005).

[101] N. Astrakhantsev, V. Braguta, and A. Kotov, J. High Energy Phys. 04 (2017) 101.

[102] J. Günther, R. Bellwied, S. Borsanyi, Z. Fodor, S. D. Katz, A. Pasztor, and C. Ratti, EPJ Web Conf. **137**, 07008 (2017).

[103] Y. Xu, P. Moreau, T. Song, M. Nahrgang, S. A. Bass, and E. Bratkovskaya, Phys. Rev. C **96**, 024902 (2017).

[104] R. Ryblewski and W. Florkowski, Phys. Rev. C **85**, 064901 (2012).

[105] I. Newton and J. Colson, *The Method of Fluxions and Infinite Series: With Its Application to the Geometry of Curve-Lines* (Printed by Henry Woodfall and sold by John Nourse, London, 1736).

[106] J. Raphson, *Analysis aequationum universalis, seu, ad aequationes algebraicas resolvendas methodus generalis, & expedita, ex nova infinitarum serierum methodo, deducta ac demonstrata* (Braddyll, London, 1697).

[107] J. Cleymans, H. Oeschler, K. Redlich, and S. Wheaton, Phys. Rev. C **73**, 034905 (2006).

[108] M. Reiter, A. Dumitru, J. Brachmann, J. A. Maruhn, H. Stoecker, and W. Greiner, Nucl. Phys. A **643**, 99 (1998).

[109] W. Cassing and E. L. Bratkovskaya, Phys. Rep. **308**, 65 (1999).

[110] Y. Akiba *et al.* (E802 Collaboration), Nucl. Phys. A **610**, 139 (1996).

[111] R. Lacasse *et al.* (E877 Collaboration), Nucl. Phys. A **610**, 153 (1996).

[112] S. Ahmad, B. E. Bonner, C. S. Chan, J. M. Clement, S. V. Efremov, E. Efstathiadis, S. E. Eiseman, A. Etkin, K. J. Foley, R. W. Hackenburg, M. A. Kramer, S. J. Lindenbaum, R. S. Longacre, W. A. Love, J. Marx, G. S. Mutchler, E. D. Platner, A. C. Saulys, L. S. Schroeder, H. W. Themann *et al.*, Phys. Lett. B **382**, 35 (1996); **386**, 496(E) (1996).

[113] J. Barrette *et al.* (E877 Collaboration), Phys. Rev. C **63**, 014902 (2001).

[114] S. Albergo, R. Bellwied, M. Bennett, D. Boemi, B. Bonner, H. Caines, W. Christie, S. Costa, H. J. Crawford, M. Cronqvist, R. Debbe, J. Engelage, I. Flores, L. Greiner, T. Hallman, G. Hijazi, G. Hoffmann, H. Z. Huang, T. J. Humanic, A. Insolia *et al.*, Phys. Rev. Lett. **88**, 062301 (2002).

[115] C. Alt *et al.* (NA49 Collaboraion), Phys. Rev. C **73**, 044910 (2006).

[116] C. Alt *et al.* (NA49 Collaboration), Phys. Rev. C **77**, 024903 (2008).

[117] C. Alt *et al.* (NA49 Collaboration), Phys. Rev. C **78**, 034918 (2008).

[118] S. V. Afanasiev *et al.* (NA49 Collaboration), Phys. Rev. C **66**, 054902 (2002).

[119] T. Anticic *et al.* (NA49 Collaboration), Phys. Rev. Lett. **93**, 022302 (2004).

[120] T. Anticic *et al.* (NA49 Collaboration), Phys. Rev. C **83**, 014901 (2011).

[121] T. Anticic *et al.* (NA49 Collaboration), Phys. Rev. C **86**, 054903 (2012).

[122] L. Ahle *et al.* (E917 and E866 Collaborations), Phys. Lett. B **476**, 1 (2000).

[123] L. Ahle *et al.* (E917 and E866 Collaboration), Phys. Lett. B **490**, 53 (2000).

[124] I. G. Bearden *et al.* (BRAHMS Collaboration), Phys. Rev. Lett. **94**, 162301 (2005).

[125] I. Arsene *et al.* (BRAHMS Collaboration), Phys. Rev. C **72**, 014908 (2005).

[126] S. S. Adler *et al.* (PHENIX Collaboration), Phys. Rev. C **69**, 034909 (2004).

[127] G. Agakishiev *et al.* (STAR Collaboration), Phys. Rev. Lett. **108**, 072301 (2012).

[128] R. Cutler and D. W. Sivers, Phys. Rev. D **17**, 196 (1978).

[129] H. U. Bengtsson and G. Ingelman, Comput. Phys. Commun. **34**, 251 (1985).

[130] M. Gell-Mann, Phys. Rev. **125**, 1067 (1962).

[131] M. D. Schwartz, *Quantum Field Theory and the Standard Model* (Cambridge University Press, Cambridge, UK, 2014).

[132] R. Mertig, M. Böhm, and A. Denner, Comput. Phys. Commun. **64**, 345 (1991).

[133] V. Shtabovenko, R. Mertig, and F. Orellana, Comput. Phys. Commun. **207**, 432 (2016).